1   **Improving PM$_{2.5}$ forecast over China by the joint adjustment of initial conditions**

2   **and source emissions with an ensemble Kalman filter**

3   Zhen Peng[1,2], Zhiquan Liu[2], Dan Chen[2,3], Junmei Ban[2]

4   1 School of Atmospheric Sciences, Nanjing University, Nanjing, China

5   2 National Center for Atmospheric Research, Boulder, Colorado, USA

6   3 Institute of Urban Meteorology, CMA, Beijing, China

8   **Abstract.** In an attempt to improve the forecasting of atmospheric aerosols, the

9   ensemble square root filter algorithm was extended to simultaneously optimize the

10 chemical initial conditions and emission input. The forecast model, which was

11 expanded by combining the Weather Research and Forecasting with Chemistry

12 (WRF-Chem) model and a forecast model of emission scaling factors, generated both

13 chemical concentration fields and emission scaling factors. The forecast model of

14 emission scaling factors was developed by using the ensemble concentration ratios of

15 the WRF-Chem forecast chemical concentrations and also the time smoothing

16 operator. Hourly surface fine particulate matter (PM$_{2.5}$) observations were assimilated

17 in this system over China from 5 to 16 October 2014. A series of 48-h forecasts were

18 then carried out with the optimized initial conditions and emissions on each day at

19 0000 UTC and a control experiment was performed without data assimilation. Besides,

20 we also performed an experiment of pure assimilation chemical ICs and the

21 corresponding 48-h forecasts experiment for comparison. The results showed that the

22 forecasts with the optimized initial conditions and emissions typically outperformed

23 those from the control experiment. In the Yangtze River delta (YRD) and the Pearl

24 River delta (PRD) regions, large reduction of the Root Mean Square Errors (RMSEs)

25 was obtained for almost the entire 48-h forecast range attributed to assimilation.

26 Especially, the relative reduction in RMSE due to assimilation was about 37.5% at

27 nighttime when WRF-Chem performed comparatively worse. In the Beijing–Tianjin–

28 Hebei (JJJ) region, relatively smaller improvements were achieved in the first 24-h

29 forecast but then no improvements were achieved afterwards. Comparing to the

30 forecasts with only the optimized ICs, the forecasts with the joint adjustment were

31 always much better during the night in the PRD and YRD regions. However, they
32 were very similar during daytime in both regions. Also, they performed similarly for
33 almost the entire 48-h forecast range in the JJJ region.
34
1. Introduction

36 Aerosol prediction by regional air quality model in heavy polluted regions is
37 challenging due to many factors. In addition to the deficiency of chemistries, the
38 uncertainties of primary and precursor emissions and the initial conditions (ICs) also
39 limit the forecast accuracy. Data assimilation (DA), which is used to improve the ICs
40 of aerosols and to optimize data on aerosol emissions, has been shown to be one of
41 the most effective ways to improve the forecasting of aerosol pollution.

42   From the perspective of reducing the uncertainties in the ICs for aerosols, recent
43 efforts have focused on assimilating aerosol observations using optimal interpolation
44 (Collins et al., 2001; Yu et al., 2003; Adhikary et al., 2008; Tombette et al., 2009; Lee
45 et al., 2013) or variational (Kahnert, 2008; Zhang et al., 2008; Benedetti et al., 2009;
46 Pagowski et al., 2010; Liu et al., 2011; Schwartz et al., 2012; Li et al., 2013; Jiang et
47 al., 2013; Saide et al., 2013) DA algorithms. Ensemble-based DA algorithms, such as
48 the ensemble Kalman filter (EnKF) (Sekiyama et al., 2010; Schutgens et al., 2010a,
49 2010b; Pagowski and Grell, 2012; Dai et al., 2014; Rubin et al., 2016; Ying, X.M., et
50 al., 2016; Yumimoto et al., 2016) and the hybrid variational-ensemble DA approach
51 (Schwartz et al., 2014) have also been applied to aerosol predictions. All these studies
52 have shown that DA is one of the most effective ways of improving aerosol
53 forecasting through assimilating aerosol observations from multiple sources (e.g.
54 ground-based observations and satellite measurements) to update the chemical ICs.

55   Numerous studies have used DA approaches to estimate or improve source
56 emissions. The EnKF is one of the most popular DA algorithms used to improve
57 estimates of aerosols and gas-phase emissions, such as NO_x, volatile organic
58 compounds, and SO_2 (van Loon et al., 2000; Heemink and Segers, 2002; Zhang et al.,
59 2005; Barbu et al., 2009; Sekiyama et al., 2010; Huneeus et al., 2012; Schutgens et al.,
60 2012; Huneeus et al., 2012, 2013; Miyazaki et al., 2014). Variational DA algorithms

have also been applied to constrain emissions of air pollution, such as black carbon, organic carbon, dust, NH_3, SO_x and NO_x (Hakami et al., 2005; Elbern et al., 2007; Henze et al., 2007, 2009; Yumimoto et al., 2007, 2008; Dubovik et al., 2008; Wang et al., 2012; Guerrette and Henze, 2015). These studies have indicated that DA can efficiently reduce the uncertainty in the emission inventories and lead to improvements in the forecasting of air quality (Mijling and van der A, 2012).

The optimization of chemical ICs and pollution emissions can improve aerosol forecasts and therefore further improvements are likely to be achieved by simultaneously optimizing the chemical ICs and emissions. Tang et al. (2011) reported that the simultaneous adjustment of the ICs of O_3, NO_x and volatile organic compounds and the emissions of NO_x and volatile organic compounds produced overall better performance in both the 1-h and 24-h ozone forecasts than the adjustment of pure ICs or emissions. Miyazaki et al. (2012) reported that the simultaneous adjustment of emissions and concentrations is a powerful approach to correcting the tropospheric ozone budget and profile analyses.

We developed a system to adjust the chemical ICs and source emissions jointly within an EnKF system coupled to the Weather Research and Forecasting with Chemistry (WRF-Chem) model (Grell et al., 2005). We then applied this system to assimilate hourly surface $PM_{2.5}$ measurements over China in early October 2014.

The remainder of the paper is organized as follows. Section 2 describes this DA system in detail and Section 3 describes the $PM_{2.5}$ observations. Then the experimental designs are introduced in Section 4. Finally, the surface $PM_{2.5}$ observations assimilation results are presented in section 5 before concluding in section 6.

2. Methodology

2.1 Forecast model

For a chemical model like WRF-Chem, the emissions are the model forcing (or boundary condition), rather than model states. Therefore, a forecasting model, **M**, was developed to forecast the emission scaling factors (representing emissions) as

91   well as the aerosol concentrations. This model combines the WRF-Chem model and

92   the forecast model of emission scaling factors.

93

94   2.1.1 WRF-Chem model

95   Version 3.6.1 of the WRF-Chem model (Grell et al., 2005) was used to forecast the

96   aerosol and chemical species. WRF-Chem is an online model with the fully coupled

97   chemical and meteorological components.

98   Most of the WRF-Chem settings were the same as those reported in Liu et al.

99   (2011): the Goddard Chemistry Aerosol Radiation and Transport (GOCART) aerosol

100   scheme coupled with the Regional Atmospheric Chemistry Mechanism for gaseous

101   chemical mechanisms; the WRF single-moment five-class microphysics scheme; the

102   Rapid Radiative Transfer Model longwave and Goddard shortwave radiation schemes;

103   the Yonsei University (YSU) boundary layer scheme; the Noah land surface model;

104   and the Grell-3D cumulus parameterization. For the GOCART aerosol scheme, the

105   aerosol species include 14 defined aerosol species and a 15th variable representing

106   unspectiated aerosol contributions (P_{25}). The 14 defined aerosol species are sulfate,

107   hydrophobic and hydrophilic organic carbon (OC_1 and OC_2 , respectively),

108   hydrophobic and hydrophilic black carbon (BC_1 and BC_2, respectively), dust in five

109   particle size bins (effective radii of 0.5, 1.4, 2.4, 4.5 and 8.0 μm; referred to as D_1,

110   D_2, D_3, D_4 and D_5, respectively) and sea salt in four particle size bins (effective

111   radii of 0.3, 1.0, 3.25 and 7.5 μm for dry air; referred to as S_1, S_2, S_3 and S_4,

112   respectively).

113   Figure 1 illustrates the model computational domain. It has 120*120 horizontal

114   grid scales at a 40.5 km spacing by the lambert conform map projection centered at

115   (35°N, 105°E). There are 57 vertical levels with the model top at 10 hPa, about 12

116   layers within the planetary boundary layer (among them the lowest 8 layers were

117   under 500 m), and the first layer centered at ~12 m.

118   With respect to the emissions, the hourly prior anthropogenic emissions were

119   based on the monthly regional emission inventory in Asia (Zhang et al., 2009) for the

120   year 2006 interpolated to the model grid. The power generator emissions were

121 interpolated for the lowest eight vertical levels (Woo et al., 2003; de meij et al., 2006;

122 Wang et al., 2010). Other anthropogenic emissions were assigned totally to the 1st

123 level. Emissions are very small above 500 m for all pollutants. In order to keep

124 objective for the prior anthropogenic emissions, no time variation was added. Thus,

125 the hourly prior anthropogenic emissions were constant. The biogenic (Guenther et al.,

126 1995), dust (Ginoux et al., 2001), dimethylsulfide and sea salt emissions (Chin et al.,

127 2000, 2002) were calculated online.

128

129 2.1.2 Forecast model of scaling factors

130 As no suitable dynamic model was available to forecast the emission scaling factors, a

131 persistence forecasting operator served as the forecast model for the scaling factors,

132 similar to the method used by Peng et al. (2015) for CO_2 emission inversion. Figure

133 2a shows the flowchart for the persistence forecasting operator $\mathbf{M}_{SF}$.

134  If the ensemble members of the updated chemical fields $\mathbf{C}^a_{i,t-1}$ (the subscript i

135 refers to the ith ensemble member, the superscript a refers to the analysis, and t

136 refers to the time) and the forecast emissions $\mathbf{E}^f_{i,t-1}$ (the superscript f refers to the

137 forecast) in the previous assimilation cycle are known, then the chemical fields $\mathbf{C}^f_{i,t}$

138 at time t can be generated via WRF-Chem (Figure 2b). In the actual process, $\mathbf{C}^f_{i,t}$

139 were available in the previous assimilation cycle, so we did not need to perform the

140 ensemble forecasts again. A dotted box was used in Figure 2a to indicate that the

141 ensemble forecasts were not performed in real process. The ensemble concentration

142 ratios $\mathbf{\kappa}_{i,t}, (i = 1, ..., N)$ are then calculated using

143
$$\mathbf{\kappa}_{i,t} = \frac{\mathbf{C}^f_{i,t}}{\overline{\mathbf{C}^f_t}}, (i = 1, ..., N), (1)$$

144 where $\overline{\mathbf{C}^f_t} = \frac{1}{N}\sum_{i=1}^{N}\mathbf{C}^f_{i,t}$ is the ensemble mean of the forecast. The ensemble mean of

145 $\mathbf{\kappa}_{i,t}$ is,

146
$$\overline{\mathbf{\kappa}_t} = \frac{1}{N}\sum_{i=1}^{N}\mathbf{\kappa}_{i,t} = \frac{1}{N}\sum_{i=1}^{N}\mathbf{C}^f_{i,t}/\overline{\mathbf{C}^f_t} = 1, (2)$$

147 so $\mathbf{\kappa}_{i,t}$ are numbers distributed around 1 and with ensemble mean values of 1.

148   The ensemble spreads of $\kappa_{i,t}, (i = 1, ..., N)$ may be small and therefore

149   covariance inflation is used to maintain them at a certain level:

150     $$(\kappa_{i,t})_{\text{inf}} = \beta(\kappa_{i,t} - \overline{\kappa_t}) + \overline{\kappa_t}, (i = 1, ..., N), (3)$$

151   In Peng et al. (2015), the CO_2 DA system worked comparatively well when the

152   ensemble spread of $\lambda_{i,t}^{a}$ ranged from 0.05 to 1.25 for $\beta = 60, 70, 75, 80$. The

153   assimilated CO2 fluxes deviated markedly from the "true" CO2 fluxes when the

154   ensemble spread of $\lambda_{i,t}^{a}$ were too small for $\beta = 10, 50$ or when the ensemble spread

155   of $\lambda_{i,t}^{a}$ were too large for $\beta = 100$. Therefore, in this work, $\beta = 1.5$ was chosen to

156   make ensure the ensemble spread of $(\kappa_{i,t})_{\text{inf}}$ ranged from 0.1 to 1.25. Same as $\kappa_{i,t}$,

157   the ensemble mean values of $(\kappa_{i,t})_{\text{inf}}$ are 1. It is noted that perhaps there are very

158   few negative values for $(\kappa_{i,t})_{\text{inf}}$ after inflation. A quality control procedure is

159   performed for $(\kappa_{i,t})_{\text{inf}}$ before further appliance. All these negative data were set as

160   0.001 in this work. There was no special reason to set them as 0.001. It is also fine to

161   set them as 0. Then $(\kappa_{i,t})_{\text{inf}}$ were re-centered to ensure the ensemble mean values of

162     $(\kappa_{i,t})_{\text{inf}}$ were all 1.

163   As the concentrations were closely related to the emissions both locally and in

164   the upwind regions and there is no suitable dynamic model available to forecast the

165   emission scaling factors, the inflated concentration ratios $(\kappa_{i,t})_{\text{inf}}$ serve as the prior

166   emission scaling factors $\lambda_{i,t}^{p}$:

167     $$\lambda_{i,t}^{p} = (\kappa_{i,t})_{\text{inf}}, (i = 1, ..., N), (4)$$

168   The above equation is not supported according to the mass conservation equation

169   but just for the purpose to generate the ensemble emissions. Same as $(\kappa_{i,t})_{\text{inf}}$, $\lambda_{i,t}^{p}$

170   are numbers distributed around 1. From the perspective of generating the ensemble

171   emissions, they can play the same role as other data, such as the random numbers

172   created by using the standard normal distribution function. However, there are

173   correlations among the grid-points of $(\kappa_{i,t})_{\text{inf}}$ because $(\kappa_{i,t})_{\text{inf}}$ are calculated

174   through a short-term forecast of WRF-Chem. Thus, $\lambda_{i,t}^{\mathrm{p}}$ have the same correlations

175   as $(\kappa_{i,t})_{\mathrm{inf}}$. While, the random numbers are totally different. There are no

176   correlations unless they are generated under certain correlations.

177   To incorporate the useful information from the previous times, the previous DA

178   cycles' analysis scaling factors, $\lambda_{i,t-M+1}^{\mathrm{a}}$, $\cdots$, $\lambda_{i,t-2}^{\mathrm{a}}$, $\lambda_{i,t-1}^{\mathrm{a}}$ and the prior scaling

179   factor $\lambda_{i,t}^{\mathrm{p}}$ were used to estimate $\lambda_{i,t}^{\mathrm{f}}$ by the time smooth operator; namely,

180     $\lambda_{i,t}^{\mathrm{f}} = \frac{1}{M}\left(\sum_{j=t-M+1}^{t-1}\lambda_{i,j}^{\mathrm{a}} + \lambda_{i,t}^{\mathrm{p}}\right), (\, i = 1, \ldots, N, j = t - M + 1, \ldots, t - 1),$ (5)

181   Here, M is the time window of the smooth operator. In this study, a value of $M = 4$

182   (hours) was chosen. According to the smooth operator, the ensemble mean values of

183     $\lambda_{i,t}^{\mathrm{f}}$ depend on the ensemble mean of $\lambda_{i,t-M+1}^{\mathrm{a}}$, $\cdots$, $\lambda_{i,t-2}^{\mathrm{a}}$, $\lambda_{i,t-1}^{\mathrm{a}}$, $\lambda_{i,t}^{\mathrm{p}}$, where the

184   ensemble means of $\lambda_{i,t}^{\mathrm{p}}$ are all 1. After multiple iterations, the smooth operator can

185   give comparatively good estimation for $\lambda_{i,t}^{\mathrm{f}}$ since anthropogenic emissions are stable

186   at a certain time scale (Mijling et al., 2012). It is a compromise between prescribed

187   prior emissions and letting the system propagate all observation information from one

188   step to the next without any guidance (Peters et al., 2007), for the case $M = 4$.

189   The ensemble members of the emissions were calculated according to

190     $$\mathbf{E}_{i,t} = \lambda_{i,t}\mathbf{E}_{t}^{\mathrm{p}}, (i = 1, \ldots, N),\ (6)$$

191   where $\mathbf{E}_{i,t}$ is the ith ensemble member of the emissions for each grid at time t, $\lambda_{i,t}$

192   represents the scaling factors and $\mathbf{E}_{t}^{\mathrm{p}}$ is the prescribed emission, which can be

193   obtained from the emission inventories. It is noted that the correlations among the

194   grid-points of the prior emissions depend on $\lambda_{i,t}^{\mathrm{p}}$. These correlations may deviate far

195   from the truth but we have no other suitable substitute. However, the correlations

196   among the grid-points of the forecast emissions should be more or less close to the

197   truth due to the appliance of the smooth operator after multiple iterations.

198   It is noted although the method is very similar to that used by Peters et al. (2007)

199   and Peng et al. (2015) for CO_2 emission inversion, it is still of novelty for applications

200 in aerosol anthropogenic emissions. In Peters et al. (2007), $\lambda_{i,t}^{\mathrm{p}}$ were all 1. And only

201 natural CO_2 emissions (i.e., biospheric and oceanic emissions) were assimilated at the

202 ecological scale due to the 'signal-to-noise' problem. Thus, the uncertainty of

203 anthropogenic and other CO_2 emissions were ignored. Besides, the framework is more

204 advanced compared to our previous work. In Peng et al. (2015), in order to generate

205 $\lambda_{i,t}^{\mathrm{p}}$, a set of ensemble forecasts were performed from time t to t+1 to produce the CO_2

206 concentration fields, forced by the prescribed net CO_2 surface fluxes with the previous

207 assimilated concentration fields as initial conditions. That means that the ensemble

208 forecast were performed twice in that DA system and it was time consuming.

209 However, in order to save computing time, we used the chemical fields $\mathbf{C}_{i,t}^{\mathrm{f}}$ available

210 in the previous assimilation cycle to calculate $\lambda_{i,t}^{\mathrm{p}}$ in this work. Thus, WRF-Chem

211 runs to forecast only once during a DA cycle.

212

2.2 Ensemble square root filter

214 The ensemble square root filter (EnSRF) algorithm was introduced by Whitaker

215 and Hamill (2002) and its expansion to analyzing aerosol ICs was described by

216 Schwartz et al. (2014). The traditional EnKF with perturbed observations (Evensen

217 1994) introduces sampling errors by perturbing the observations. In contrast to the

218 traditional EnKF, the EnSRF (Whitaker and Hamill, 2002) and the Ensemble

219 Adjustment Kalman Filter (EAKF, developed by Anderson, 2001) obviate the need to

220 perturb the observations. The local ensemble Kalman filtering (LEKF), a kind of

221 EnSRF, was presented by Ott et al. (2002, 2004). It was computationally more

222 efficient compared to the traditional EnKF, since it simultaneously assimilates the

223 observations within a spatially local volume independently. The local Ensemble

224 Transform Kalman Filter (LETKF, Hunt, 2007) integrates the advantages of the

225 Ensemble Transform Kalman Filter (ETKF, developed by Bishop et al., 2001) and the

226 LEKF. The computational cost of LETKF is much lower than that of the original

227 LEKF because the former does not require an orthogonal basis. Though LETKF has

228 more advantages, we still chose the same EnSRF as Schwartz et al. (2014) because we

229 did not need to extend it to analyzing aerosol ICs, very similar to Schwartz et al.

230 (2014).

231   Following the notation of Ide et al. (1997), given an m-dimensional background

232 model forecast vector $\mathbf{x}^b$, a p-dimensional observation vector $\mathbf{y}^o$ and an operator $\mathbf{H}$

233 that converts the model state to the observation states, we expressed the variables as

234 an ensemble mean (denoted by an over-bar) and a deviation from the mean (denoted

235 by a prime). Thus, the ensemble mean $\bar{\mathbf{x}}^a$ of the analyzed state $\mathbf{x}^a$ and the

236 deviations $\mathbf{x}'^a$ from the ensemble mean are updated separately by

237
$$\bar{\mathbf{x}}^a = \bar{\mathbf{x}}^b + \mathbf{K}(\mathbf{y}^o - \mathbf{H}\bar{\mathbf{x}}^b), \quad (7)$$

238
$$\mathbf{x}'^a = \mathbf{x}'^b + \widetilde{\mathbf{K}}(\mathbf{y}'^o - \mathbf{H}\mathbf{x}'^b), \quad (8)$$

239 where $\mathbf{K}$ is the traditional Kalman gain matrix and $\widetilde{\mathbf{K}}$ is the gain used to update the

240 deviations from the ensemble mean. These are given by

241
$$\mathbf{K} = \mathbf{P}^b\mathbf{H}^T(\mathbf{H}\mathbf{P}^b\mathbf{H}^T + \mathbf{R})^{-1}, \quad (9)$$

$$\widetilde{\mathbf{K}} = \mathbf{P}^b\mathbf{H}^T\left[\left(\sqrt{\mathbf{H}\mathbf{P}^b\mathbf{H}^T + \mathbf{R}}\right)^{-1}\right]^T \left(\sqrt{\mathbf{H}\mathbf{P}^b\mathbf{H}^T + \mathbf{R}} + \sqrt{\mathbf{R}}\right)^{-1}$$

242
$$= \left(1 + \sqrt{\mathbf{R}/(\mathbf{H}\mathbf{P}^b\mathbf{H}^T + \mathbf{R})}\right)^{-1} \mathbf{K}, \quad (10)$$

243 where $\mathbf{P}^b = \frac{1}{N-1}\sum_{i=1}^{N}\mathbf{x}'^b(\mathbf{x}'^b)^T$ is the $m*m$-dimensional background error

244 covariance matrix and $\mathbf{R}$ is the $p*p$-dimensional diagonal observation error

245 covariance matrix. In real applications, $\mathbf{P}^b\mathbf{H}^T$ and $\mathbf{H}\mathbf{P}^b\mathbf{H}^T$ will be approximated

246 using the background ensemble; namely,

247
$$\mathbf{P}^b\mathbf{H}^T = \frac{1}{N-1}\sum_{i=1}^{N}\mathbf{x}'^b(\mathbf{H}\mathbf{x}'^b)^T \quad (11)$$

248
$$\mathbf{H}\mathbf{P}^b\mathbf{H}^T = \frac{1}{N-1}\sum_{i=1}^{N}\mathbf{H}\mathbf{x}'^b(\mathbf{H}\mathbf{x}'^b)^T. \quad (12)$$

249 In equations (11) and (12), N is the ensemble size.

250   Note that for the joint analysis of ICs and emissions, the state vector $\mathbf{x}$ is the

251 joint vector of the mass concentration $\mathbf{C}$ and the emission scaling factor $\boldsymbol{\lambda}$, i.e.

252 $\mathbf{x} = [\mathbf{C}, \boldsymbol{\lambda}]^T$. In this study, the state variables of the analysis of the ICs were the 15

253 WRF-Chem/GOCART aerosol variables, same as that reported by Schwartz et al.

254 (2012). The state variables of the emission scaling factors include $\boldsymbol{\lambda}_{PM2.5}$, $\boldsymbol{\lambda}_{SO2}$, $\boldsymbol{\lambda}_{NO}$

255 and λ_{NH3} and are described in section 2.3.1. After each ensemble analysis, the

256 ensemble forecasts were performed with the corresponding models to advance **C** and

257 $\boldsymbol{\lambda}$ to the next analysis time.

258   In this work, a 50-member ensemble was chosen, following Schwartz et al.

259 (2012) and Whitaker and Hamill (2002). Covariance localization forced EnSRF

260 analysis increments to zero 1280 km from an observation in the horizontal and one

261 scale height to reduce spurious correlations due to sampling error for all control

262 variables, similar to Pagowski et al., (2012) and Schwartz et al., (2012, 2014). In

263 addition, posterior (after assimilation) multiplicative inflation following Whitaker and

264 Hamill (2012) was applied aiming to maintain ensemble spread for only the

265 concentration analysis. The inflation factor $\alpha = 1.2$ was chosen as Pagowski et al.,

266 (2012) and Schwartz et al., (2012, 2014). Additive or prior inflation was not employed.

267 As for the emission scaling factor $\boldsymbol{\lambda}$, the inflation was not used at this step.

268

269 **2.3 Data assimilation system**

270 2.3.1 State variables

271   As stated in section. 2.2, the state variables of the analysis of the ICs were the 15

272 WRF-Chem/GOCART aerosol variables. The $PM_{2.5}$ observation operator was the

273 same as that described by Schwartz et al. (2012) and expressed as

$$\mathbf{y}^f = \boldsymbol{\rho}_d[\mathbf{P_{25}} + 1.375\mathbf{S} + 1.8(\mathbf{OC_1} + \mathbf{OC_2}) + \mathbf{BC_1} + \mathbf{BC_2}$$

274 $$+\mathbf{D_1} + 0.286\mathbf{D_2} + \mathbf{S_1} + 0.942\mathbf{S_2}], \quad (13)$$

275 where $\boldsymbol{\rho}_d$ represents the dry air density, which is multiplied by the mixing ratios of

276 aerosol species (in $\mu g \cdot kg^{-1}$) to convert the units to $\mu g\ m^{-3}$ for consistency with the

277 observations.

278   From the perspective of the optimization of emissions, four species of emission

279 scaling factors ($\lambda_{PM2.5}$, λ_{SO2}, λ_{NO} and λ_{NH3}) were also considered as the state

280 variables of the DA system. Atmospheric inorganic aerosols are not only from the

281 primary emissions, but also from secondary processes- chemical and thermodynamic

282 transformations from the gas-phase precursors. Therefore, not only the primary

283 sources of $PM_{2.5}$, but also the sources of the gas-phase precursors, need to be

284 optimized. In this study, the sources of SO_2, NO_x and NH_3 ($\mathbf{E}_{SO2}$, $\mathbf{E}_{NO}$ and $\mathbf{E}_{NH3}$),

285 which have a large impact on the distribution of $PM_{2.5}$, were also optimized in

286 addition to the primary sources of $PM_{2.5}$. It is noted that for the optimization of the

287 emission scaling factors, $\mathbf{M}_{SF}$ serves as the forecast model and the observation

288 operator reflects the combined information of emissions (in the format of $\boldsymbol{\lambda}$ in

289 equation (6)), the physics and chemistry processes in WRF-Chem simulations and the

290 transformation $PM_{2.5}$ from model space to observation space (equation (13)).

291   The direct sources of $PM_{2.5}$ include the unspeciated primary sources of $PM_{2.5}$

292 $\mathbf{E}_{PM2.5}$, sulfate $\mathbf{E}_{SO4}$, nitrate $\mathbf{E}_{NO3}$, organic compounds E_{org} and elemental

293 compounds E_{BC}; all of them are given in two modes (the nuclei and accumulation

294 modes, represented as i and j in the subscripts respectively). The ratios between the

295 nuclei and accumulation modes were the same as in the suggested emission process

296 for National Emission Inventory in WRF-Chem (Freitas et al., 2011). The formula of

297 sulfate and nitrate emissions in the model are as below:

$$\mathbf{E}_{PM2.5i} : \mathbf{E}_{PM2.5j} = 1:4, \quad (14)$$

$$\mathbf{E}_{SO4i} : \mathbf{E}_{SO4j} = 1:4, \quad (15)$$

$$\mathbf{E}_{NO3i} : \mathbf{E}_{NO3j} = 1:4, \quad (16)$$

$$\mathbf{E}_{SO4i} + \mathbf{E}_{SO4j} = a * (\mathbf{E}_{PM2.5i} + \mathbf{E}_{PM2.5j} - \mathbf{E}_{EC} - \mathbf{E}_{ORG}), \quad (17)$$

$$\mathbf{E}_{NO3i} + \mathbf{E}_{NO3j} = b * (\mathbf{E}_{PM2.5i} + \mathbf{E}_{PM2.5j} - \mathbf{E}_{EC} - \mathbf{E}_{ORG}), \quad (18)$$

303 where $\mathbf{E}_{EC}$ represents elemental carbon and $\mathbf{E}_{ORG}$ organic compounds, and

304 $a = 0.074$ and $b = 0.038$ were chosen based on the internal emissions and

305 observational data. In the DA process, the first 6 species of direct sources of

306 emissions ($\mathbf{E}_{PM2.5i}$, $\mathbf{E}_{PM2.5j}$, $\mathbf{E}_{SO4i}$, $\mathbf{E}_{SO4j}$, $\mathbf{E}_{NO3i}$, and $\mathbf{E}_{NO3j}$), which may have

307 larger uncertainties in heavy polluted events, were updated according to the variation

308 of $\boldsymbol{\lambda}_{PM2.5}$. $\mathbf{E}_{PM2.5i}$ and $\mathbf{E}_{PM2.5j}$ were directly updated according to the variation in

309 $\boldsymbol{\lambda}_{PM2.5}$. The emissions ($\mathbf{E}_{SO4i}$, $\mathbf{E}_{SO4j}$, $\mathbf{E}_{NO3i}$ and $\mathbf{E}_{NO3j}$) were also updated according

310 to the variations in $\mathbf{E}_{PM2.5i}$ and $\mathbf{E}_{PM2.5j}$.

311      $\mathbf{E}_{EC}$ and $\mathbf{E}_{ORG}$ of the anthropogenic emissions were not assimilated, which is a

312 limitation in this work. Besides, emissions of dust and sea salt were not assimilated. It

313 is true that these emissions are also important for the atmosphere aerosol. The reason

314 we did not assimilate $\mathbf{E}_{EC}$ and $\mathbf{E}_{ORG}$ is that only the PM$_{2.5}$ measurements are used in

315 this DA experiment. However, the sources of the aerosols (especially organic aerosols)

316 are so complex that our knowledge of their formation mechanisms is far from clear.

317 Though it is technically possible to have all emissions assimilated, with such limited

318 observations adding more control variables would cause much more uncertainties in

319 the system which might lead to unreasonable analysis.

320

321 2.3.2 Procedure for the DA system

322 Figure 2 (b) shows the workflow of the DA system. The steps in this workflow are as

323 follows.

324   (1) The persistence forecasting operator $\mathbf{M}_{SF}$ is applied to forecast the

325 background fields of the emission scaling factors $\boldsymbol{\lambda}_{PM2.5}^{f}$, $\boldsymbol{\lambda}_{SO2}^{f}$, $\boldsymbol{\lambda}_{NO}^{f}$ and $\boldsymbol{\lambda}_{NH3}^{f}$. The

326 forecast chemical fields of P$_{25}$, SO$_2$, NO and NH$_3$ of the previous assimilation cycle

327 are used to create the prior emission scaling factors $\boldsymbol{\lambda}_{PM2.5}^{p}$, $\boldsymbol{\lambda}_{SO2}^{p}$, $\boldsymbol{\lambda}_{NO}^{p}$ and $\boldsymbol{\lambda}_{NH3}^{p}$.

328 The background scaling factors are then generated using equation (5).

329   (2) The ensemble members of the emissions, $\mathbf{E}_{PM2.5i}^{f}$, $\mathbf{E}_{PM2.5j}^{f}$, $\mathbf{E}_{SO2}^{f}$, $\mathbf{E}_{NO}^{f}$ and

330 $\mathbf{E}_{NH3}^{f}$, are prepared according to equation (6). The corresponding emissions of $\mathbf{E}_{SO4i}^{f}$,

331 $\mathbf{E}_{SO4j}^{f}$, $\mathbf{E}_{NO3i}^{f}$ and $\mathbf{E}_{NO3j}^{f}$ are obtained based on equations (15–18). Other inorganic

332 species of the anthropogenic emission, such as $\mathbf{E}_{EC}$ and $\mathbf{E}_{ORG}$, are not perturbed for

333 WRF-Chem. However, other anthropogenic emissions, such as $\mathbf{E}_{PM2.5}$, $\mathbf{E}_{SO4}$ and

334 $\mathbf{E}_{NO3}$, are much larger than $\mathbf{E}_{EC}$ and $\mathbf{E}_{ORG}$ in most area of China, and the ensemble

335 spreads of the aerosol concentrate largely dependent on the uncertainties of those

336 anthropogenic emissions. Besides, model errors raised from the meteorology, the

337 emission and the chemical model itself are compensated to some extent through the

338 use of multiplicative inflation. In other words, the ensemble spread of the

339 concentrations can be kept at a certain level though $\mathbf{E}_{EC}$ and $\mathbf{E}_{ORG}$, are not

340 perturbed.

341   Natural emissions, such as dust and sea salt emissions were not perturbed

342   explicitly when the forecast emissions were generated. However, emissions of dust

343   and sea salt were parameterized within the GOCART model (Chin et al., 2002).

344   Within the DA system, varying meteorology across the members implicitly perturbed

345   dust and sea salt emissions.

346   (3) Forced by the changed emissions ($\mathbf{E}_{PM2.5i}$, $\mathbf{E}_{PM2.5j}$, $\mathbf{E}_{SO2}$, $\mathbf{E}_{NO}$, $\mathbf{E}_{NH3}$,

347    $\mathbf{E}_{SO4i}$, $\mathbf{E}_{SO4j}$, $\mathbf{E}_{NO3i}$ and $\mathbf{E}_{NO3j}$ were substituted by $\mathbf{E}_{PM2.5i}^{f}$, $\mathbf{E}_{PM2.5j}^{f}$, $\mathbf{E}_{SO2}^{f}$, $\mathbf{E}_{NO}^{f}$,

348    $\mathbf{E}_{NH3}^{f}$, $\mathbf{E}_{SO4i}^{f}$, $\mathbf{E}_{SO4j}^{f}$, $\mathbf{E}_{NO3i}^{f}$ and $\mathbf{E}_{NO3j}^{f}$; the other emissions such as $\mathbf{E}_{EC}$ and $\mathbf{E}_{ORG}$

349   remained unchanged), WRF-Chem is run again to forecast the chemical fields $\mathbf{\rho}^{f}$

350   with the updated chemical fields of the previous assimilation cycle as the ICs. The

351   state variables, i.e., 15 aerosol species and four scaling factors, are then prepared.

352   (4) The model-simulated PM$_{2.5}$ concentration at the observation space is then

353   calculated via equation (13). At this time, the state vector $\mathbf{x}^{f} = [\mathbf{C}^{f}, \mathbf{\lambda}^{f}]^{T}$ was

354   prepared.

355   (5) In the assimilation step, the state variables, the concentrations of 14 defined

356   aerosol species and a 15th unspeciated aerosol, and the four species of emission

357   scaling factors $\mathbf{\lambda}_{PM2.5}^{f}$, $\mathbf{\lambda}_{SO2}^{f}$, $\mathbf{\lambda}_{NO}^{f}$ and $\mathbf{\lambda}_{NH3}^{f}$, were optimized through EnSRF.

358   (6) After the assimilation step, the optimized emissions ($\mathbf{E}_{PM2.5i}^{a}$, $\mathbf{E}_{PM2.5j}^{a}$, $\mathbf{E}_{SO2}^{a}$,

359    $\mathbf{E}_{NO}^{a}$, $\mathbf{E}_{NH3}^{a}$, $\mathbf{E}_{SO4i}^{a}$, $\mathbf{E}_{SO4j}^{a}$, $\mathbf{E}_{NO3i}^{a}$ and $\mathbf{E}_{NO3j}^{a}$) were calculated according to equations

360   (6, 15–18) using the optimized scaling factors ($\mathbf{\lambda}_{PM2.5}^{a}$, $\mathbf{\lambda}_{SO2}^{a}$, $\mathbf{\lambda}_{NO}^{a}$ and $\mathbf{\lambda}_{NH3}^{a}$).

361

362   **3. PM$_{2.5}$ observation data and errors**

363   Hourly averaged surface PM$_{2.5}$ observations from the Ministry of Environmental

364   Protection of China were assimilated. There were altogether 876 national control

365   measurement sites over China. The PM$_{2.5}$ observation sites spanned most of central

366   and eastern China but were primarily located in urban and suburban areas. So it

367   always happened that there were more than one observation sites in certain city,

368   which were fall into the same model grid. Since we did not know the exact

369   observation environment of the sites, we randomly selected one observation site in a

370   city for assimilation experiment and one for verification purposes to ensure that there

371   was at most one assimilated measurements for one model grid. Altogether 77 stations

372   were selected for the $PM_{2.5}$ assimilation experiment and another 77 independent

373   stations were selected for verification. Figure 1 shows the locations of 77

374   measurement sites used for the $PM_{2.5}$ assimilation experiment and 77 independent

375   sites used for forecast verification.

376   The observation error covariance matrix **R** in equation (9) includes

377   contributions from measurement and representation errors. Similar to the work of

378   Schwartz et al. (2012), the measurement error ε_0 is defined as $\varepsilon_0 = 1.5 + 0.0075 *$

379   Π_0, where Π_0 denotes the observational values for $PM_{2.5}$ ($\mu g\ m^{-3}$). Thus, higher

380    $PM_{2.5}$ values were associated with larger measurement errors. Following Elbern et al.

381   (2007) and Pagowski et al. (2010), Schwartz et al. (2012), the representativeness error

382   ε_r depends on the resolution of the model and the characteristics of the observation

383   locations and is calculated as $\varepsilon_r = r\varepsilon_0\sqrt{\Delta x/\mathrm{L}}$, where r is an adjustable parameter

384   (here, $r = 0.5$), Δx is the grid spacing (here, 40.5 km), and L is the radius of

385   influence of an observation (here, L was set to 3 km following Elbern et al. (2007),

386   since we do not know the station type that used in this work). The total $PM_{2.5}$ error (ε_t)

387   is defined as $\varepsilon_t = \sqrt{{\varepsilon_0}^2 + {\varepsilon_r}^2}$. The observation errors are assumed to be uncorrelated

388   so that **R** is a diagonal matrix.

389   The $PM_{2.5}$ observations were subject to quality control to ensure data reliability

390   before DA. Considering that China has had intense pollution events, $PM_{2.5}$ values

391   larger than 800 $\mu g\ m^{-3}$ were classified as unrealistic and were not assimilated;

392   observations with the ensemble mean of the first guess departure exceeding 100

393    $\mu g\ m^{-3}$ were also omitted, following Schwartz et al. (2012). The numbers of the

394   observations were about 17700. Among them 8 observations were discarded because

395   they were larger than 800 $\mu g\ m^{-3}$ and 243 (around 1.5%) were discarded due to the

396   latter reasons.

397

4. Experimental design

Two parallel experiments were performed to evaluate the impact of PM$_{2.5}$ DA on the analyses and forecasts of aerosols over China: an assimilation experiment and a control experiment. Both experiments used identical WRF-Chem settings and physical parameterizations.

4.1 Spin-up ensemble forecast with perturbed Initial and boundary conditions

The initialization and spin-up procedures were identical to those reported by Schwartz et al. (2014). The ICs and lateral boundary conditions (LBCs) for the meteorological fields were provided by the National Centers for Environmental Prediction Global Forecast System (GFS).

The initial meteorological fields were created at 0000 UTC 1 October 2014 by interpolating the GFS analyses onto the model domain. The 50 ensemble members were then generated by adding Gaussian random noise with a zero mean and static background error covariances (Torn et al., 2006) to the temperature, water vapor, velocity, geopotential height and dry surface pressure fields. The ICs of each member were zero in the initial aerosol fields, representing clean conditions as described by Liu et al. (2011).

The LBCs for the meteorological fields were then interpolated from the GFS analyses from 0000 UTC 1 October 2014 to 0000 UTC 16 October 2014 and perturbed similarly to the initial fields at 0000 UTC 1 October 2014. The aerosol LBCs of each member for all experiments were idealized profiles embedded within the WRF/Chem model.

Fifty-member emissions were created by adding random noise to the anthropogenic emissions, same as reported by Schwartz et al. (2014),

$$\mathbf{E}^*_{ip}(\eta, t) = \mathbf{E}_p(\eta, t) + \mathbf{W}_{ip}\boldsymbol{\sigma}^{\mathrm{E}}_p(\eta, t)$$

where $\mathbf{E}^*_{ip}(\eta, t)$ is the ith ensemble member for the pth emissions variable at the ηth grid point and the tth hour, $\mathbf{E}_p$ is the unperturbed emissions. The term $\boldsymbol{\sigma}^{\mathrm{E}}_p$ is

425   the standard deviation of all $\mathbf{E}_p$ values and in the horizontally adjacent points of grid

426   box η at and within 2 h of t. $\boldsymbol{W}$ is a weight that was randomly drawn from a

427   standard Gaussian distribution and varied for each ensemble member and variable but

428   was spatially and temporally constant. No correlations between emissions variables

429   were considered, which was a limitation of this approach. For possible negative

430   perturbed emissions, they were set as $\mathbf{E}_{ip}^*(\eta, t) = 0.001 * \mathbf{E}_p(\eta, t)$. This will increase

431   the prescribed emissions more or less. However, only very few data were negative. So,

432   this influence can be negligible.

433   Before the first DA cycle, a 50-member ensemble of four-day WRF-Chem

434   forecasts was performed from 0000 UTC 1 October to 2300 UTC 4 October 2014

435   using the perturbed ICs at 0000 UTC 1 October 2014, the corresponding perturbed

436   LBCs and the emissions. Then a 50-member ensemble aerosol forecasts at 0000 UTC

437   5 October 2014 were produced.

438

439   4.2 Assimilation experiments

440   Two DA experiments were performed. One was the pure assimilation of chemical ICs

441   (hereafter expC), the others was the joint adjustment of chemical ICs and source

442   emissions (hereafter expJ). Both DA experiments had same settings except for the

443   emissions. They were conducted from 0000 UTC 5 October 2014 to 0000 UTC 16

444   October 2014. The assimilation cycle interval was 1 h.

445   In the first DA cycle in expJ, the first 50 ensemble chemical fields were drawn

446   from the WRF-Chem ensemble forecasts valid at 0000 UTC 5 October 2014, as

447   described in section 4.1. Using the ensemble aerosol forecasts, the prior emission

448   scaling factors $\boldsymbol{\lambda}_{i,t}^{\mathrm{p}}$ at 2300 UTC 4 October 2014 were calculated. $\boldsymbol{\lambda}_{i,t}^{\mathrm{p}}$ were used

449   directly as $\boldsymbol{\lambda}_{i,t}^{\mathrm{f}}$ for the first 5 assimilation cycles (after 5 assimilation cycles, the

450   system has been initialized, all future scaling factors could be created using the

451   persistence forecasting operator $\mathbf{M}_{\mathrm{SF}}$). Then, the state vector $\mathbf{x}^{\mathrm{f}} = [\mathbf{C}^{\mathrm{f}}, \boldsymbol{\lambda}^{\mathrm{f}}]^{\mathrm{T}}$ was

452   prepared. And after that, the DA cycle started.

453   In expC, the first chemical fields were also drawn from the WRF-Chem

454   ensemble forecasts valid at 0000 UTC 5 October 2014. Then, the state vector

455    $\mathbf{x}^f = [\mathbf{C}^f]^T$ was prepared and the DA cycle started.

456   At the WRF-Chem forecast step of the subsequent assimilation cycles for both

457   experiments, the ICs for the chemical variables of each member were drawn from the

458   updated chemical fields of the previous cycle. The aerosol LBCs of each member for

459   all experiments were idealized profiles embedded within the WRF/Chem model. As

460   for the meteorological ensemble fields, the LBCs were prepared in advance as

461   depicted in section 4.1; the ICs of each member of the meteorological fields were

462   drawn from the forecast meteorological fields of the previous cycle before

463   re-centering with the GFS analysis because we do not do meteorological analysis:

$$464 \qquad \boldsymbol{\pi}_{i_{\text{new}}} = \boldsymbol{\pi}_i + (\boldsymbol{\pi}_{\text{GFS}} - \overline{\boldsymbol{\pi}}), \quad (18)$$

465   where $\boldsymbol{\pi}_i$ is the ith member of the forecast meteorological fields of the previous

466   cycle, $\overline{\boldsymbol{\pi}}$ is the ensemble mean of the forecast meteorological fields of the previous

467   cycle, $\boldsymbol{\pi}_{\text{GFS}}$ is the meteorological field interpolated from the GFS analyses and

468    $\boldsymbol{\pi}_{i_{\text{new}}}$ is the new meteorological field used as the IC in WRF-Chem in the next cycle.

469   As stated in the first paragraph in this section, the settings of expC were the same

470   as those in expJ except for the emissions. In expJ, the ensemble anthropogenic

471   emissions were generated by using emission scaling factors. While in expC, the

472   ensemble anthropogenic emissions were prepared by adding random noise, as stated

473   in 4.1.

474

475   4.3 Control experiment

476   The control experiment was conducted for the same period as the assimilation

477   experiment and the simulation cycle period was 1 h, as in the assimilation experiment.

478   The first initial chemical fields were extracted from the ensemble mean valid at 0000

479   UTC 5 October 2014. In the subsequent simulation process, the ICs for the chemical

480   fields were from the previous cycle's 1-h forecast. The LBCs and ICs for the

481   meteorological fields were updated by interpolating the GFS analyses. The emissions

482   were the prescribed emissions $\mathbf{E}_t^p$ without any perturbation.

483

5. Results

Statistics for both expJ and expC were computed using the ensemble mean prior (background) and posterior (analysis) fields (average of the 50-member ensemble). The ensemble performances were first examined. Output from the first day of the cycling DA configurations was excluded from all verification statistics to allow the ensemble fields to ''spin up'' from the initial ensemble.

As the measurement coverage is an important factor that may determine the performance in DA, we primarily focused our attention on the results from three sub-regions with comparatively dense observational coverage (Figure 1): the Beijing–Tianjin–Hebei region (JJJ, 12 stations for assimilation and 12 stations for verification); the Yangtze River delta (YRD, 24 stations for assimilation and 24 stations for verification); and the Pearl River delta (PRD, 9 stations for assimilation and 9 stations for verification).

5.1 Ensemble performance

It is important to assess the ensemble performance for an ensemble-based DA system. In a well-calibrated system, a comparison of the prior ensemble mean root-mean-square error (RMSE) with respect to the observations should equal the prior "total spread" (square root of the sum of ensemble variance and observation error variance) (Houtekamer et al., 2005). Figure 3 shows the time series for the prior ensemble mean RMSE and the total spread for $PM_{2.5}$ aggregated over all observations in the three sub-regions for expJ. It indicates that the magnitudes of both the total spread and the RMSE were influenced by the diurnal cycle and heavy air pollution. Almost all the total spreads were smaller than the RMSE, showing an insufficient spread of $PM_{2.5}$ ensemble forecasts, which is especially evident for heavy polluted period with much larger RMSEs. For expC, the characteristics of the prior ensemble mean RMSE and the total spread for $PM_{2.5}$ were very similar to that for the joint DA experiment.

The magnitudes of the ensemble spread of the emission scaling factors of the

513 joint DA experiment were important for emission inversion. They were very stable

514 throughout the ~10 day experiment period, which indicates that $\mathbf{M}_{SF}$ can generate

515 stable artificial data to generate the ensemble emissions. For $\boldsymbol{\lambda}^{f}_{PM2.5}$, they ranged

516 from 0.25 to 1 in most model area. Figure 3d shows the area-averaged time series

517 extracted from the ensemble spread of $\boldsymbol{\lambda}^{f}_{PM2.5}$. It shows that the ensemble spread was

518 stably distributed around 0.5, which indicates that the uncertainty of the ensemble

519 emissions was about 50%.

520

521 5.2 Impact on aerosol ICs

522 To evaluate quantitatively the impact of the ensemble assimilation system on the ICs,

523 the mean errors (bias), RMSEs and correlation coefficient (CORR) of the assimilation

524 experiment and the control run were first analyzed. These statistics were calculated

525 against independent observations over all the analyses from 6 to 16 October 2014.

526 Table 1 shows that the bias magnitudes of the control run were 15.9 and 20.6 $\mu g\ m^{-3}$

527 for the YRD and the PRD, respectively, suggesting a significant overestimation of the

528 WRF-Chem aerosol mass in these two sub-regions. However, a significant

529 underestimation of the aerosol mass occurred in the JJJ region, where the model bias

530 was $-18.0\ \mu g\ m^{-3}$. The RMSEs of the control run were 81.6, 30.6 and 31.8 $\mu g\ m^{-3}$ for

531 the JJJ, YRD and PRD regions, respectively. After assimilation, the statistics showed

532 an apparent improvement and the magnitude of the bias and the RMSE decreased for

533 both DA experiment. For expJ, both the maximum bias and the RMSE were obtained

534 in the JJJ region, and were -10.3 and 66.9 $\mu g\ m^{-3}$, respectively. The CORR increased

535 from 0.79, 0.60, and 0.62 to 0.83, 0.85, and 0.80 for the JJJ, YRD and PRD,

536 respectively. The statistics of expC were very similar to those of expJ. The bias and

537 the RMSE in the JJJ region were -12.2 and 64.0 $\mu g\ m^{-3}$, respectively. And the CORR

538 were 0.85, 0.80, and 0.80 for the JJJ, YRD and PRD, respectively. These results

539 indicate that the initial $PM_{2.5}$ fields can be adjusted efficiently by the EnSRF.

540 It is interesting to note that expC has better RMSE and CORR than expJ but poor

541 bias in JJJ. And expC has better bias and RMSE than expJ but poor CORR in PRD.

542 Maybe small number of samples caused the uncertainties of the statics. However, the

543   differences were very small. The analysis of both experiments were very similar.

544   Then the analysis increments (i.e. $\bar{\mathbf{x}}^a - \bar{\mathbf{x}}^b$) were investigated to show the direct

545   impact of PM$_{2.5}$ DA. They are determined by both the observation increments and the

546   relative magnitudes of the forecast error and the observation error, based on Equation

547   (7). From Figure 4(a), (e) and (f), the increments of both assimilation experiments

548   were distributed around the observations as expected. However, the impact of

549   assimilating PM$_{2.5}$ observations was not limited to the areas where observations were

550   located, observations information was also transported to other areas through the

551   WRF-Chem forecast. Besides, the ensemble forecasts also partly contributed to the

552   spatial distribution of the PM$_{2.5}$ mass. Therefore, the spatial distributions of the PM$_{2.5}$

553   mass in both assimilation experiments were significantly different from the control

554   run (see Figure 4(b), (c) and(d)), which suggest that assimilation PM$_{2.5}$ observations

555   impacts greatly on the aerosol ICs. The PM$_{2.5}$ mass magnitude of both assimilation

556   experiments were smaller than that of the control run at the lowest model level in the

557   YRD, the PRD and in central China. Conversely, positive differences (analysis minus

558   control) were gained in the JJJ region and in northeast China. These indicated the

559   reduction of the overestimation or underestimation of the WRF-Chem simulation over

560   these regions with data assimilation.

561

562   5.3 Impact on emissions

563   To determine the impact of assimilating PM$_{2.5}$ observations on the chemical emissions,

564   we analyzed the area-averaged time series extracted from the forecast emission

565   scaling factors, the optimized emission scaling factors, the prior emissions and the

566   optimized emissions. Figure 5 shows that $\boldsymbol{\lambda}^f_{PM2.5}$ were changed along with $\boldsymbol{\lambda}^a_{PM2.5}$.

567   This indicates that observation information ingested from the previous observations

568   was incorporated through the usage of the time smooth operator.

569   Figure 5 also shows that although the prior emissions $\mathbf{E}^p_{PM2.5}$ had no diurnal

570   variation when the experiments were designed, the optimized PM$_{2.5}$ scaling factor,

571     $\boldsymbol{\lambda}^a_{PM2.5}$, showed an obvious variation with time, as did the optimized unspeciated

572   primary sources of PM$_{2.5}$, $\mathbf{E}^a_{PM2.5}$. Moreover, the values of $\boldsymbol{\lambda}^a_{PM2.5}$ were <1 at almost

573   all times in the YRD and PRD, which resulted that the analyzed emission $\mathbf{E}^a_{PM2.5}$

574   were lower than the prior PM$_{2.5}$ emissions $\mathbf{E}^p_{PM2.5}$. In the YRD, the prior $\mathbf{E}^p_{PM2.5}$ was

575   about 0.127 μg m^{-2} s^{-1} over all hours. After assimilation, the time-averaged optimized

576   $\mathbf{E}^a_{PM2.5}$ decreased to 0.107 μg m^{-2} s^{-1}, about 15.6% lower than the prior value. In the

577   PRD, the prior $\mathbf{E}^p_{PM2.5}$ was about 0.10 μg m^{-2} s^{-1}. The time-averaged optimized

578   $\mathbf{E}^a_{PM2.5}$ decreased to 0.066 μg·m^{-2} s^{-1}, leading to a decrease of 35.0%. However,

579   larger values for the optimized $\mathbf{E}^a_{PM2.5}$ were obtained in the JJJ region in three

580   periods, from 1600 UTC 6 October to 0000 UTC 8 October, from 1600 UTC 9

581   October to 0000 UTC 10 October, and from 1600 UTC 13 October to 0000 UTC 15

582   October as a result of the increased optimized scaling factor $\boldsymbol{\lambda}^a_{PM2.5}$. This may have

583   been caused by the burning of crop residues during harvesting in this region (Li et al.,

584   2016), which was not taken into account in the prior emissions. However, the PM$_{2.5}$

585   measurements network was still spatially sparse and heterogeneous in this work.

586   Almost all measurements were located in the city and no data available in the rural.

587   Meanwhile, the crop residues burning always occur in the rural region. Therefore, the

588   PM$_{2.5}$ measurements network can only capture the burning information a few hours

589   later. Hence, although the system is able to detect the emission changes caused by

590   burning events, the time that the system started to show increased scaling factors

591   might be not accurate enough (may shift a few hours later). Maybe a Kalman

592   smoother would have been a better system to solve this problem.

593   The NO, SO$_2$ and NH$_3$ emissions were all adjusted to some extent by our DA

594   approach (see Figure 6). The NO emissions increased by 41.3, 43.7 and 20.3% in the

595   JJJ, YRD and PRD regions, respectively. The SO$_2$ emissions increased by 16.3, 10.0

596   and 18.3% and the NH$_3$ emissions increased by 16.7, 7.8 and 7.5% in the JJJ, YRD

597   and PRD regions, respectively.

598   Figure 7 shows the spatial distribution of the time-averaged scaling factors

599   $\boldsymbol{\lambda}^a_{PM2.5}$ at the lowest model level over all hours from 6 to 16 October 2014, since the

600   emissions at higher levels were so small that the impact of assimilating PM$_{2.5}$

601 observations was negligible. Figure 8 shows the distribution of $\mathbf{E}_{PM2.5}^{p}$ and the

602 time-averaged differences between the ensemble mean of the assimilation and the

603 prior values.

604   These patterns are consistent with those in Figure 5. Negative differences were

605 obtained in most areas of the YRD and PRD, indicating that the $PM_{2.5}$ DA primarily

606 decreased the $PM_{2.5}$ emissions. Conversely, positive differences were obtained in

607 South Hebei, North Henan and Southeast Shanxi provinces, indicating that DA

608 increased the $PM_{2.5}$ emissions.

609   As the economy in China has developed, the spatiotemporal distribution of

610 emissions has changed as a result of changes in energy consumption, the structure of

611 the energy market and advances in technology. Therefore although this inventory of

612 emissions may have correctly described anthropogenic emissions in 2006 when it was

613 constructed, it is not representative of the anthropogenic emissions in 2014.

614 Theoretically, the assimilated emissions should reduce the uncertainty in the prior

615 emissions as a result of the application of observations. Different from the situations

616 that standard national emission inventories were reported by government in USA,

617 European or other countries, the rapid economic development and complexity of

618 emission sources in China lead to large uncertainties in the current emission

619 inventories even for the latest version. Thus it's impossible for us to conduct the direct

620 evaluation on emissions.

621   Although we had no direct emission observations to evaluate the analyzing

622 emissions, which was a challenging to many emission inversion research teams (e.g.

623 Tang et al, 2011; Miyazaki et al., 2012; Ding et al., 2015; Mclinden et al., 2016; etc.),

624 the improvement of emissions can be verified in terms of two aspect, the diurnal

625 variation and the location of increased emissions. The diurnal variation in the

626 assimilated emissions verified this statement to some extent. Especially in the PRD

627 and YRD, $\mathbf{E}_{PM2.5}^{a}$ in the daytime were always larger than those in the night, which

628 agreed well with Olivier et al. (2003), the WRAP (2006) and Wang et al. (2010). In

629 addition, the locations of the larger values for the optimized $E_{PM2.5}^{a}$ in the JJJ region

630 was in good agreement with the place of the crop residues burning *traced by the*

631 environmental satellite of China. There were 10, 231, 37 and 3

632 crop residue burning spots in Hebei, Henan, Shandong and Shanxi province

633 respectively from 5 to 11 October 2014 and 7, 20, 5 and 21 respectively from 12 to 18

634 October 2014 (Weekly Crop Residue Burning Monitoring Report traced by

635 Environmental Satellite, 2015a, 2015b).

636   However, the analysis emissions are only a mathematical optimum. They are

637 influenced greatly by the model errors and the observation errors. In addition, only

638 surface $PM_{2.5}$ observations were applied in this work, which may lack abundant

639 constraint on the sources of the secondary aerosol precursors. More observations are

640 needed to obtain reliable emissions for the sources of the gas-phase precursors.

641

642 5.4 Verification of aerosol forecasting

643   For the assimilation experiment, 48-h forecasts were performed at each 0000

644 UTC from 6 to 16 October 2014 with the hourly forecast output for both assimilation

645 experiments. For the verification forecasting experiment for expJ (hereafter fcJ), the

646 ensemble mean of the analyzed ICs and emissions of expJ were used in this

647 longer-range model forecast. For the verification forecasting experiment for expC

648 (hereafter fcC), the ensemble mean of the analyzed ICs of expC and the prescribed

649 anthropogenic emissions were used.

650   In order to get a more visualized picture of the impact of DA for both

651 assimilation experiments, time series of the hourly $PM_{2.5}$ extracted from the analysis

652 (AN), the control run (CT) and the hourly output of 48-h forecast (fc24 for the first

653 day forecast and fc48 for the second day forecast) were compared with the

654 observations (OBS) for three megacities Beijing, Shanghai and Guangzhou,

655 respectively (Figure 9). As expected, the time series of the analysis (also the

656 background) were consistent with the observations. The control run showed large

657 deviations from the observations, especially in Shanghai and Guangzhou. Benefit

658 from DA on both the first day and the second day forecasts can be clearly seen.

659   The bias and the RMSE of the surface $PM_{2.5}$ forecasts as a function of forecast

660 range was then calculated against the independent observations for the three

661 sub-regions (Figure 10). Both the bias and the RMSEs of the control run were

662 characterized by the diurnal cycle in the YRD and PRD. The largest errors were seen

663 at 2100 UTC in the YRD (about 29 $\mu g \cdot m^{-3}$ for bias and 37 $\mu g \cdot m^{-3}$ for RMSEs) and at

664 2300 UTC in the PRD (about 36 $\mu g \cdot m^{-3}$ for bias and 41 $\mu g \cdot m^{-3}$ for RMSEs), likely

665 indicating significant systematic forecast errors at these times. From 0300 to 0900

666 UTC, the bias (about 1 $\mu g \cdot m^{-3}$ in the YRD and -5 $\mu g \cdot m^{-3}$ in the PRD) and the RMSE

667 values (about 14 $\mu g \cdot m^{-3}$ in the YRD and 16 $\mu g \cdot m^{-3}$ in the PRD) were much smaller

668 than at other times in both the YRD and PRD, showing that WRF-Chem performed

669 well during this period. However, in the JJJ region, the bias (about -20 $\mu g \cdot m^{-3}$) and

670 the RMSEs (about 50 $\mu g \cdot m^{-3}$) were always large as a result of a heavy pollution event.

671 After assimilation, both the magnitude of the bias and the RMSEs decreased sharply.

672 Especially in in YRD and PRD, most bias ranged from -5 to 5 $\mu g \cdot m^{-3}$ and most

673 RMSEs ranged from 11 to 14 $\mu g \cdot m^{-3}$, further indicating that DA greatly affected the

674 ICs.

675 The improvements in the surface PM$_{2.5}$ forecasts by the joint adjustment of the

676 ICs and emissions were very large in the YRD and PRD for expJ. Large reduction of

677 the magnitude of the bias and the RMSEs due to assimilation can be seen for almost

678 the entire 48-h forecast range. From 10- to 23-h and from 34- to 47-h, in particular,

679 the relative reduction in RMSE was about 37.5%. However, the DA impact was much

680 smaller for 3- to 9-h forecast ranges, which are at daytime of the first day forecast. In

681 addition, the improvements were nearly negligible in PRD from 27- to 33-h, the

682 daytime of the second day forecast, suggesting that the benefit gained from adjusting

683 the ICs decreased progressively and eventually disappeared with model integration.

684 And the performance was actually deteriorated in YRD during the same time. One of

685 the possible reasons was that chemical model performed sufficiently well during

686 daytime when the boundary layer was unstable and therefore the further improvement

687 was more difficult. And there were always large errors during the night when the

688 boundary layer was stable, so that large improvements could be obtained. The other

689 possible reason can be attributed to the a priori constant emissions. The differences

690   between the optimized $PM_{2.5}$ emissions and the prior emissions were comparatively

691   small during the day, but the optimized $PM_{2.5}$ emissions were much smaller than the a

692   prior emissions during the night. So that the control run could performed worse during

693   the night and it could performed well during the day. Given the a priori variable

694   emissions provided, the control run will perform better during the night. Nevertheless,

695   attributed greatly to the large adjustment of chemical emissions, substantial

696   improvements were still achieved from 34- to 47- h. These results revealed that joint

697   adjustment of the ICs and emissions can improve surface $PM_{2.5}$ forecasts up to 48 h in

698   the YRD and PRD.

699   As for expC, it seemed that large improvements in the surface $PM_{2.5}$ forecasts

700   were gained through the adjustment of the ICs in PRD from 10- to 23-h and from 34-

701   to 47-h. Large reduction of the magnitude of the bias and the RMSEs due to

702   assimilation can be seen during this period. The relative reduction in RMSE ranged

703   from 25% to 37.5%. However, the forecasts deviated much from the observations for

704   3- to 9-h and 27- to 33-h forecast ranges. One of the reason may be that the

705   adjustment of the ICs decreased the analysis field too much on the whole since the

706   WRF-Chem forecast aerosol mass was systematically overestimated in PRD (see

707   Figure 4, Figure 9f and Figure 10e). While this aerosol mass overestimation might be

708   also due to the possibly overestimated emissions in some time periods (not all-day

709   long) which are not corrected in the simulation. So the over-adjusted ICs compensated

710   the unadjusted emissions in some period but also lead to the negative biases for the

711   periods when emission is not overestimated or underestimated. The other factor was

712   the diurnal variation. It is very clear that $PM_{2.5}$ mass gradually decreased with time

713   from 0000 UTC to 0008 UTC and then obtained the smallest value. After that it

714   increased with time from 0009 UTC to 0023 UTC obtained the largest value at about

715   0000 UTC. Both reasons led to the systematically underestimation of $PM_{2.5}$ mass of

716   fcC from 3- to 9-h and from 27- to 33-h, though maybe the aerosol ICs were very

717   close to the observations. Therefore, both the magnitude of the bias and the RMSEs of

718   the fcC were larger than those of the control run. In addition, $PM_{2.5}$ forecasts of the

719   fcC were benefit much from the diurnal variation and the adjustment of the ICs from

720 10- to 23-h and from 34- to 47-h. As a consequence, the magnitude of the

721 corresponding bias and the RMSEs of the fcC were smaller than those of the control

722 run. Similar statics characteristics were also gained in YRD. But the improvements

723 were comparatively small from 10- to 23-h and from 34- to 47-h. However, the

724 performance of fcJ was much better than that of fcC during the night in PRD and

725 YRD. While in the daytime, the improvement of expJ seems to be not so big or even

726 negligible. This could be attributed much to the emissions since the ICs of both

727 forecasts were very similar. In the forecast experiment of expC, the emissions were

728 the default monthly anthropogenic emissions. While in the forecast experiment of

729 expJ, the assimilated emissions were much smaller than the default anthropogenic

730 emissions in almost all the night in both regions indicating that the prior emission

731 uncertainties might be the dominating reasons that cause biases between observed and

732 model simulated concentrations in these cases. In the daytime in PRD, the assimilated

733 emissions were a little smaller than the default anthropogenic emissions. But in the

734 daytime in YRD, the assimilated emissions were a little larger than the default

735 anthropogenic emissions for most time (see Figure 5). While those changes between

736 assimilated emissions and prior emissions in the daytime are not as significant as that

737 in the nighttime.

738   Both DA systems did not perform as well in the JJJ region as in the YRD and

739 PRD. Relatively smaller improvements were achieved in the first 24-h forecast but

740 then no improvements were achieved afterwards in JJJ. One possible reason for this

741 result may be systematic errors due to chemistry mechanism in WRF-Chem. The

742 sources of the aerosols are so complex that our knowledge of their formation

743 mechanisms is far from clear and large uncertainties still exist in the model

744 simulations. Chemical transport models have a tendency to underestimate PM

745 concentrations, especially during episodes of heavy pollution (Denby et al., 2007) due

746 to some missing reactions (Wang et al., 2014; Zhang et al., 2015, Zheng et al., 2015;

747 Chen et al., 2016). Another reason can be attributed to the forecast meteorological

748 fields. There were still large uncertainties, especially when boundary layer was stable

749 and the wind speed was very small during episodes of heavy pollution. As a result, a

750 large bias may be obtained in forecasts of heavy pollution given the ICs and emission

751 inventories achieved from the joint assimilation. Another reason may be the sparse

752 coverage of measurements. There were only 12 sites in the JJJ region (Figure 1) and

753 the measurement coverage was much sparser than in the YRD or PRD.

754

6. Summary and Discussion

756 The EnSRF algorithm was extended to adjust the chemical ICs and the primary

757 and precursor emissions to improve forecasts for surface $PM_{2.5}$. This system was

758 applied to assimilate hourly surface $PM_{2.5}$ measurements from 5 to 16 October 2014

759 over China. To evaluate the effectiveness of DA, 48-h forecasts were performed using

760 the optimized ICs and emissions, together with a control experiment without DA.

761 Besides, the experiment of pure assimilation chemical ICs and the corresponding 48-h

762 forecasts experiment were also performed for comparison. The results indicated that

763 the forecasts with the optimized ICs and emissions performed much better than the

764 control simulations. Large improvements were achieved for almost all the 48-h

765 forecasts, particularly in the YRD and PRD. However, it did show some

766 improvements in the first 24-h but then there is no difference between the control run

767 and the forecasts in the JJJ region afterwards, which may be attributed to the sparse

768 measurement coverage and the deficiencies in the model system for forecasting heavy

769 pollution. Comparing to the forecasts with only the optimized ICs, the forecasts with

770 the joint adjustment were always much better during the night in the PRD and YRD

771 regions. However, they were very similar during daytime in both regions. And in the

772 JJJ region, they performed similarly for almost the entire 48-h forecast range.

773 There are still some limitations in this study. Firstly, we use the default monthly

774 anthropogenic emissions as the prior emissions and no time variation was added to

775 keep objective, since no resolution of temporal allocations at shorter but critical

776 (e.g.,day-of-week, diurnal) scales is available. As shown in earlier work, the constant

777 emissions will worsen the chemical forecasts (de Meij et al., 2006; Wang et al, 2009).

778 For the joint DA system itself, it cannot benefit from the constant prior anthropogenic

779 emissions. But the normalized RMSE in Figure 10g decreased due to the poor

780 forecasts of control run. The control run will perform better when variable emissions

781 within the day are allowed, especially during the night. As a result, the relative

782 reduction in RMSE could not be so large during the night. Secondly, no correlations

783 between emissions variables were considered when perturbing the emissions, which

784 will lead to the reduction of the correlations between the variables. Thus, the chemical

785 forecast will deviate from the truth to some degree. Fortunately, the perturbed

786 emissions were only used in the initialization and spin-up experiment and expC.

787 Therefore, there were no impacts on expJ and the control run except for expC. Thirdly,

788 $\mathbf{E_{EC}}$ and $\mathbf{E_{ORG}}$ are not perturbed in expJ. However, as stated in Sect. 2.3.2, the

789 ensemble spread of $\mathbf{OC_1}$ and $\mathbf{OC_2}$ can be kept at a certain level. As a result, $\mathbf{OC_1}$

790 and $\mathbf{OC_2}$ changed much contributed to the $PM_{2.5}$ assimilation in expJ, which

791 suggests that the influence of not perturbing $\mathbf{E_{EC}}$ and $\mathbf{E_{ORG}}$ could be negligible. But,

792 because of the too small magnitudes of $\mathbf{BC_1}$ and $\mathbf{BC_2}$, the differences (assimilation

793 minus control) of $\mathbf{BC_1}$ and $\mathbf{BC_2}$ were nearly close to zero. Fourthly, the experiment

794 (expE) where only emissions were assimilated was not included here. But it was still

795 worth to simultaneously assimilate the chemical ICs and emission. For one thing, in

796 expE, the chemical concentrations can be updated by the WRF-Chem model

797 simulations with the assimilated emissions as the initial field in each DA cycle. That

798 means that the 50-member ensemble forecasts were performed twice and it was time

799 consuming. For another, better concentration analysis could be obtained in expJ due

800 to the simultaneous assimilation of ICs and emissions. While in expE, there may be

801 larger uncertainties for the updated chemical concentrations through WRF-Chem due

802 to the deficiency of chemistries and the uncertainties of the ICs. This will lead to

803 larger uncertainties for the emission inversion. Also the improvement of $PM_{2.5}$

804 forecasts will be limited due to the comparatively poor chemical ICs.

805   This study represents the first step in the simultaneous optimization of chemical

806 ICs and emissions and only surface $PM_{2.5}$ measurements were assimilated. In future

807 work, gas-phase observations of SO_2, NO_2 and CO will be used to further improve the

808 performance of this DA system.

809

Acknowledgements. We thank three anonymous reviews for their helpful comments. This work was supported by the National Key Technologies Research and Development program of china (2016YFC0202102), the Strategic Priority Research Program – Climate Change: Carbon Budget and Relevant Issues (XDA05040404), and the National Natural Science Foundation of China (41575141).

References

Anderson, J. L.: An Ensemble Adjustment Kalman Filter for Data Assimilation, Mon.Weather Rev., 129, 2884–2903, 2001.

Adhikary, B., Kulkarni, S., Dallura, A., Tang, Y., Chai, T., Leung, L. R., Qian, Y., Chung, C. E., Ramanathan, V., and Carmichael, G. R.: A regional scale chemical transport modeling of Asian aerosols with data assimilation of AOD observations using optimal interpolation technique, Atmos. Environ., 42, 8600–8615, doi:10.1016/j.atmosenv.2008.08.031, 2008.

Barbu, A. L., Segers, A. J., Schaap, M., Heemink, A.W., and Builtjes, P. J. H.: A multi-component data assimilation experiment directed to sulphur dioxide and sulphate over Europe, Atmos. Environ., 43, 1622–1631, 2009.

Benedetti, A., Morcrette, J., Boucher, O., Dethof, A., Engelen, R., Fisher, M., Flentje, H., Huneeus, N., Jones, L., and Kaiser, J.: Aerosol analysis and forecast in the European Centre for Medium-Range Weather Forecasts Integrated Forecast System: 2. Data assimilation, J. Geophys. Res, 114, D13205, doi:10.1029/2008JD011115, 2009.

Bishop, C. H., Etherton, B. J., and Majumdar, S. J.: Adaptive sampling with the ensemble transform Kalman filter. Part I: Theoretical aspects, Mon. Weather Rev., 129, 420–436, 2001.

Chen, D., Liu, Z., Fast, J., and Ban, J.: Simulations of sulfate–nitrate–ammonium (SNA) aerosols during the extreme haze events over northern China in October 2014, Atmos. Chem. Phys., 16, 10707-10724, doi:10.5194/acp-16-10707-2016, 2016.

Chin, M., Rood, R. B., Lin, S. J., Muller, J. F., and Thompson, A. M.: Atmospheric sulfur cycle simulated in the global model GOCART: Model description and

842   global properties, J. Geophys. Res.-Atmos., 105, 24671–24687, 2000.

843   Chin, M., Ginoux, P., Kinne, S., Torres, O., Holben, B.N., Duncan, B. N., Martin,
844   R.V., Logan, J.A., Higurashi, A., and Nakajima, J.: Tropospheric aerosol optical
845   thickness from the GOCART model and comparisons with satellite and Sun
846   photometer measurements, J. Atmos. Sci., 59(3), 461–483, 2002.

847   Collins, W. D., Rasch, P. J., Eaton, B. E., Khattatov, B. V., and J.-F. Lamarque, J.-F.:
848   Simulating aerosols using a chemical transport model with assimilation of
849   satellite aerosol retrievals: Methodology for INDOEX, J. Geophys. Res., 106,
850   7313–7336, 2001.

851   de Meij, A., Krol, M., Dentener, F., Vignati, E., Cuvelier, C., and Thunis, P.: The
852   sensitivity of aerosol in Europe to two different emission inventories and
853   temporal distribution of emissions, Atmos. Chem. Phys., 6, 4287-4309,
854   doi:10.5194/acp-6-4287-2006, 2006.

855   Dai, T., Schutgens, N.A.J., Goto, D. Shi, G.Y., Nakajima, T.: Improvement of aerosol
856   optical properties modeling over Eastern Asia with MODIS AOD assim- ilation
857   in a global non-hydrostatic icosahedral aerosol transport model, Environ. Pollut.,
858   195, 319–329, 2014.

859   Denby, B., Schaap, M., Segers, A.J., Builtjes, P.J.H., Horalek, J.: Comparison of two
860   data assimilation methods for assessing PM10 exceedances on the European
861   scale, Atmos. Environ., 42 (30), 7122–7134, 2007.

862   Ding, J., van der A, R. J., Mijling, B., Levelt, P. F., and Hao, N.: NO_x emission
863   estimates during the 2014 Youth Olympic Games in Nanjing, Atmos. Chem.
864   Phys., 15, 9399-9412, doi:10.5194/acp-15-9399-2015, 2015.

865   Dubovik, O., Lapyonok, T., Kaufman, Y. J., Chin, M., Ginoux, P., Kahn, R. A., and
866   Sinyuk, A.: Retrieving global aerosol sources from satellites using inverse
867   modeling, Atmos. Chem. Phys., 8, 209–250, doi:10.5194/acp-8-209-2008, 2008

868   Elbern, H., Strunk, A., Schmidt, H., and Talagrand, O.: Emission rate and chemical
869   state estimation by 4-dimensional variational inversion, Atmos. Chem. Phys., 7,
870   3749–3769, doi:10.5194/acp- 7-3749-2007, 2007.

871   Evensen, G.: Sequential data assimilation with a nonlinear quasi-geostrophic model

872   using Monte Carlo methods to forecast error statistcs, J. Geophys. Res., 99(C5),
873   10143–10162, 1994.

874   Freitas, S. R.; Longo, K. M.; Alonso, M. F.; Pirre, M.; Marecal, V.; Grell, G.;
875   Stockler, R.; Mello, R. F.; Sánchez Gácita, M.. PREP-CHEM-SRC 1.0: a
876   preprocessor of trace gas and aerosol emission fields for regional and global
877   atmospheric chemistry models. Geoscientific Model Development, v. 4, p.
878   419-433, 2011.

879   Ginoux, P., Chin, M. Tegen, I., Prospero, J. M., Holben, B., Dubovik, O., and Lin,
880   S.-J.: Sources and distributions of dust aerosols simulated with the GOCART
881   model, J. Geophys. Res., 106, 20,255–20,273, doi:10.1029/2000JD000053,
882   2001.

883   Grell, G., Peckham, S. E., Schmitz, R., McKeen, S. A., Frost, G., Skamarock, W. C.,
884   and Eder, B.: Fully coupled "online" chemistry within the WRF model, Atmos.
885   Environ., 39, 6957–6975, doi:10.1016/j.atmosenv.2005.04.027, 2005.

886   Guenther, A., Hewitt, C. N., Erickson, D., Fall, R., Geron, C., Graedel, T., Harley, P.,
887   Klinger, L., Lerdau, M., McKay, W., Pierce, T., Scholes, B., Steinbrecher, R.,
888   Tallamraju, R., Taylor, J., and Zimmerman, P.: A global model of natural
889   volatile organic compound emissions, J. Geophys. Res., 100, 8873–8892,
890   doi:10.1029/94JD02950, 1995.

891   Guerrette, J. J. and Henze, D. K.: Development and application of the
892   WRFPLUS-Chem online chemistry adjoint and WRFDA-Chem assimilation
893   system, Geosci. Model Dev., 8, 1857-1876, doi:10.5194/gmd-8-1857-2015,
894   2015.

895   Hakami, A., Henze, D. K., Seinfeld, J. H., Chai, T., Tang, Y., Carmichael, G. R., and
896   Sandu, A.: Adjoint inverse modeling of black carbon during the Asian Pacific
897   Regional Aerosol Characterization Experiment, J. Geophys. Res.-Atmos., 110,
898   D14301, doi:10.1029/2004JD005671, 2005.

899   Heemink, A.W., and Segers, A.J.: Modeling and prediction of environmental data in
900   space and time using Kalman filtering, Stoch. Environ. Res. Risk Assess. 16 (3),
901   225–240, 2002.

Henze, D. K., Hakami, A., and Seinfeld, J. H.: Development of the adjoint of GEOS-Chem, Atmos. Chem. Phys., 7, 2413–2433, doi:10.5194/acp-7-2413-2007, 2007.

Henze, D. K., Seinfeld, J. H., and Shindell, D. T.: Inverse modeling and mapping US air quality influences of inorganic PM2.5 precursor emissions using the adjoint of GEOS-Chem, Atmos. Chem. Phys., 9, 5877–5903, doi:10.5194/acp-9-5877-2009, 2009.

Houtekamer, P. L., Mitchell, H. L., Pellerin, G., Buehner, M., Charron, M., Spacek, L., and Hansen, B.: Atmospheric data assimilation with an ensemble Kalman filter: Results with real observations, Mon. Weather Rev., 133, 604–620, 2005.

Ide, K., Courtier, P., Ghil, M., and Lorenc, A. C.: Unified notation for data assimilation: operational, sequential and variational, J. Meteorol. Soc. Japan, 75, 181–189, 1997.

Jiang, Z., Liu, Z., Wang, T., Schwartz, C. S., Lin, H.-C., and Jiang, F.: Probing into the impact of 3DVAR assimilation of surface PM10 observations over China using process analysis, J. Geophys. Res. Atmos., 118, 6738–6749, doi:10.1002/jgrd.50495, 2013.

Peters, W., Jacobson, A. R., Sweeney, C., Andrews, A. E., Conway, T. J., Masarie, K., Miller, J. B., Bruhwiler, L. M. P., Petron, G., Hirsch, A. I., Worthy, D. E. J., van der Werf, G. R.,Randerson, J. T., Wennberg, P. O., Krol, M. C., Tans, P. P.: An atmospheric perspective on North American carbon dioxide exchange: CarbonTracker, P. Natl. Acad. Sci. USA, 104, 18925–18930, 2007.

Kahnert, M.: Variational data analysis of aerosol species in a regional CTM: Background error covariance constraint and aerosol optical observation operators, Tellus, Ser. B, 60, 753–770, doi:10.1111/j.1600-0889.2008.00377, 2008.

Kleist, D. T., Parrish, D. F., Derber, J. C., Treadon, R., Wu, W.-S., and Lord, S.: Introduction of the GSI into the NCEP global data assimilation system, Weather Forecast., 24, 1691–1705, 2009.

Huneeus, N., Chevallier, F., and Boucher, O.: Estimating aerosol emissions by assimilating observed aerosol optical depth in a global aerosol model, Atmos.

Chem. Phys., 12, 4585-4606, doi:10.5194/acp-12-4585-2012, 2012.

Huneeus, N., Boucher, O., and Chevallier, F.: Atmospheric inversion of SO2 and primary aerosol emissions for the year 2010, Atmos. Chem. Phys., 13, 6555-6573, doi:10.5194/acp-13-6555-2013, 2013.

Hunt, B., Kostelich, E., and Szunyogh, I.: Efficient data assimilation for spatiotemporal chaos: a Local Ensemble Transfom Kalman Filter, Physica D, 230, 112–126, 2007.

Lee, E.-H., Ha, J.-C., Lee, S.-S., and Chun, Y.: PM10 data assimilation over South Korea to Asian dust forecasting model with the optimal interpolation method, Asia-Pacific J. Atmos. Sci., 49(1), 73–85, doi:10.1007/s13143-013-0009-y, 2013.

Li, Z., Zang, Z., Li, Q. B., Chao, Y., Chen, D., Ye, Z., Liu, Y., and Liou, K. N.: A three-dimensional variational data assimilation system for multiple aerosol species with WRF/Chem and an application to $PM_{2.5}$ prediction, Atmos. Chem. Phys., 13, 4265-4278, doi:10.5194/acp-13-4265-2013, 2013.

Li, J., Li, Y., Bo, Y., and Xie, S.: High-resolution historical emission inventories of crop residue burning in fields in China for the period 1990–2013, Atmos. Environ., 138, 152–161, 2016.

Liu, Z., Liu, Q., Lin, H. C., Schwartz, C. S., Lee, Y. H., and Wang, T.: Three-dimensional variational assimilation of MODIS aerosol optical depth: implementation and application to a dust storm over East Asia, J. Geophys. Res., 116, D23206, doi:10.1029/2011JD016159, 2011.

Liu, F., Zhang, Q., Tong, D., Zheng, B., Li, M., Huo, H., and He, K. B.: High-resolution inventory of technologies, activities, and emissions of coal-fired power plants in China from 1990 to 2010, Atmos. Chem. Phys., 15, 13299-13317, doi:10.5194/acp-15-13299-2015, 2015.

McLinden, C.A., Fioletov, V., Shephard, M.W., Krotkov, N., Li, C., Martin, R.V., Moran, M.D., and J. Joiner,: Space-based detection of missing sulfur dioxide sources of global air pollution, Nat. Geosci., 9, 496–500, doi:10.1038/ngeo2724, 2016.

Mijling, B. and van der A, R. J.: Using daily satellite observations to estimate emissions of short-lived air pollutants on a mesoscopic scale, J. Geophys. Res., 117, D17302, doi:10.1029/2012JD017817, 2012.

Miyazaki, K., Eskes, H. J., Sudo, K., Takigawa, M., van Weele, M., and Boersma, K. F.: Simultaneous assimilation of satellite NO_2, O_3, CO, and HNO_3 data for the analysis of tropospheric chemical composition and emissions, Atmos. Chem. Phys., 12, 9545– 9579, doi:10.5194/acp-12-9545-2012, 2012.

Miyazaki, K., Eskes, H. J., Sudo, K., and Zhang, C.: Global lightning NOx production estimated by an assimilation of multiple satellite data sets, Atmos. Chem. Phys., 14, 3277–3305, doi:10.5194/acp-14-3277-2014, 2014.

Ott, E., Hunt, B. R., Szunyogh, I., Zimin, A. V., Kostelich, E. J., et al.: Exploiting local low dimensionality of the atmospheric dynamics for efficient Kalman filtering, arXiv:physics/0203058, 24 pp., available at: http://arxiv.org/abs/physics/0203058v3/, 2002.

Ott, E., Hunt, B. R., Szunyogh, I., Zimin, A. V., Kostelich, E. J., et al.: A local ensemble Kalman filter for atmospheric data assimilation, Tellus A, 56, 415–428, 2004.

Pagowski, M., Grell, G. A., McKeen, S. A., Peckham, S. E., and Devenyi, D.: Three-dimensional variational data assimilation of ozone and fine particulate matter observations: some results using the Weather Research and Forecasting – Chemistry model and Grid-point Statistical Interpolation, Q. J. Roy. Meteor. Soc., 136, 2013–2024, doi:10.1002/qj.700, 2010.

Pagowski, M., and Grell, G. A.: Experiments with the assimilation of fine aerosols using an ensemble Kalman filter, J. Geophys. Res.-Atmos., 117, D21302, doi:10.1029/2012jd018333, 2012.

Peng, Z., Zhang, M., Kou, X., Tian, X., and Ma, X.: A regional carbon data assimilation system and its preliminary evaluation in East Asia, Atmos. Chem. Phys., 15, 1087-1104, doi:10.5194/acp-15-1087-2015, 2015.

Pope, C. A.: Review: Epidemiological basis for particulate air pollution health standards, Aerosol Sci. Tech., 32, 4–14, 2000.

Pope, C. A., Burnett, R. T., Thun, M. J., Calle, E. E., Krewski, D., Ito, K., and Thurston, G. D.: Lung cancer, cardiopulmonary mortality, and long-term exposure to fine particulate air pollution, J. Am. Med. Assoc., 287, 1132–1141, 2002.

Rubin, J. I., Reid, J. S., Hansen, J. A., Anderson, J. L., Collins, N., Hoar, T. J., Hogan, T., Lynch, P., McLay, J., Reynolds, C. A., Sessions, W. R., Westphal, D. L., and Zhang, J.: Development of the Ensemble Navy Aerosol Analysis Prediction System (ENAAPS) and its application of the Data Assimilation Research Testbed (DART) in support of aerosol forecasting, Atmos. Chem. Phys., 16, 3927-3951, doi:10.5194/acp-16-3927-2016, 2016.

Saide, P. E., Carmichael, G. R., Liu, Z., Schwartz, C. S., Lin, H. C., da Silva, A. M., and Hyer, E.: Aerosol optical depth assimilation for a size-resolved sectional model: impacts of observationally constrained, multi-wavelength and fine mode retrievals on regional scale analyses and forecasts, Atmos. Chem. Phys., 13, 10425-10444, doi:10.5194/acp-13-10425-2013, 2013.

Schwartz, C. S., Liu, Z., Lin, H. C., and McKeen, S. A.: Simultaneous three-dimensional variational assimilation of surface fine particulate matter and MODIS aerosol optical depth, J. Geophys. Res., 117, D13202, doi:10.1029/2011JD017383, 2012.

Schwartz, C. S., Liu, Z., Lin, H.-C., and Cetola, J. D.: Assimilating aerosol observations with a "hybrid" variational-ensemble data assimilation system, J. Geophys. Res. Atmos., 119, 4043–4069, doi:10.1002/2013JD020937, 2014.

Sekiyama, T. T., Tanaka, T. Y., Shimizu, A., and Miyoshi, T.: Data assimilation of CALIPSO aerosol observations, Atmos. Chem. Phys., 10, 39-49, doi:10.5194/acp-10-39-2010, 2010.

Schutgens, N. A. J., Miyoshi, T., Takemura, T., and Nakajima, T.: Sensitivity tests for an ensemble Kalman filter for aerosol assimilation, Atmos. Chem. Phys., 10, 6583-6600, doi:10.5194/acp-10-6583-2010, 2010.

Schutgens, N. A. J., Miyoshi, T., Takemura, T., and Nakajima, T.: Applying an ensemble Kalman filter to the assimilation of AERONET observations in a

global aerosol transport model, Atmos. Chem. Phys., 10, 2561-2576, doi:10.5194/acp-10-2561-2010, 2010.

Schutgens, N., Nakata, M., and Nakajima, T.: Estimating Aerosol Emissions by Assimilating Remote Sensing Observations into a Global Transport Model, Remote Sensing,4, 3528-3543, 2012.

Tang, X., Zhu, J., Wang, Z. F., and Gbaguidi, A.: Improvement of ozone forecast over Beijing based on ensemble Kalman filter with simultaneous adjustment of initial conditions and emissions, Atmos. Chem. Phys., 11, 12901–12916, doi:10.5194/acp-11-12901-2011, 2011.

Tombette, M., Mallet, V., and Sportisse, B.: PM10 data assimilation over Europe with the optimal interpolation method, Atmos. Chem. Phys., 9, 57-70, doi:10.5194/acp-9-57-2009, 2009.

Torn, R. D., Hakim, G. J., and Snyder, C.: Boundary conditions for limited-area ensemble Kalman filters, Mon. Weather Rev., 134, 2490–2502, 2006.

van Loon, M., Builtjes, P. J. H., and Segers, A. J.: Data assimilation of ozone in the atmospheric transport chemistry model LOTOS, Environ. Model. Softw., 15, 603–609, 2000.

Wang, J., Xu, X., Henze, D. K., Zeng, J., Ji, Q., Tsay, S.-C., and Huang, J.: Top-down estimate of dust emissions through integration of MODIS and MISR aerosol retrievals with the GEOS-Chem adjoint model, Geophys. Res. Lett., 39, L08802, doi:10.1029/2012GL051136, 2012.

Wang, Y. X., Zhang, Q. Q., Jiang, J. K., Zhou, W., Wang, B. Y., He, K. B., Duan, F. K., Zhang, Q., Philip, S., and Xie, Y. Y.: Enhanced sulfate formation during China's severe winter haze episode in January 2013 missing from current models, J.Geophys.Res.-Atmos., 119, 10.1002/2013JD021426, 2014

Wang, X.Y., Liang,. X.Z., Jiang, W.M., Tao, Z.N., Wang, J.X.L., Liu, H.N., Han Z.W., Liu, S.Y., Zhang, Y.Y., Grell, G.A., Peckham, S.E.: WRF-Chem simulation of East Asian air quality: Sensitivity to temporal and vertical emissions distributions, Atmospheric Environment,44(2010) 660-669

Whitaker, J. S., and Hamill, T. M.: Ensemble data assimilation without perturbed

observations, Mon. Weather Rev., 130, 1913–1924, 2002.

Woo, J.H., Baek, J.M., Kim, J.W., Carmichaael, G.R., Thongboonchoo, N., Kim, S.T., An, J.H.: Development of a Multi-Resolution Emission Inventory and Its Impact on Sulfur Distribution for Northeast Asia, Water, Air, and Soil Pollution 148: 259–278, 2003.

Weekly Crop Residue Burning Monitoring Report , http://hjj.mep.gov.cn/jgjs/201510/P020151012746205487305.pdf, 2015a (in Chinese).

Weekly Crop Residue Burning Monitoring Report, http://hjj.mep.gov.cn/jgjs/201510/P020151019568921489639.pdf, 2015b (in Chinese).

Xia Y., Zhao, Y., Nielsen, C.P., Benefits of China's efforts in gaseous pollutant control indicated by the bottom-up emissions and satellite observations 2000-2014, Atmospheric Environment, 136, 43-53, 2016

Yu, H., Dickinson, R. E., Chin, M., Kaufman, Y. J., Geogdzhayev, B., and Mishchenko, M. I.: Annual cycle of global distributions of aerosol optical depth from integration of MODIS retrievals and GOCART model simulations, J. Geophys. Res., 108(D3), 4128, doi:10.1029/2002JD002717, 2003.

Yumimoto, K., Uno, I., Sugimoto, N., Shimizu, A., and Satake, S.: Adjoint inverse modeling of dust emission and transport over East Asia, Geophys. Res. Lett., 34, L00806, doi:10.029/2006GL028551, 2007.

Yumimoto, K., Uno, I., Sugimoto, N., Shimizu, A., Liu, Z., and Winker, D. M.: Adjoint inversion modeling of Asian dust emission using lidar observations, Atmos. Chem. Phys., 8, 2869-2884, doi:10.5194/acp-8-2869-2008, 2008.

Yumimoto, K., Nagao, T.M., Kikuchi, M., Sekiyama, T.T, Murakami, H.,Tanaka, T.Y., Ogi, A., Irie, H., Khatri, P., Okumura, H., Arai, K., Morino, I., Uchino, O., Maki, T.: Aerosol data assimilation using data from Himawari-8, a next-generation geostationary meteorological satellite, Geophys. Res. Lett., 43, 5886–5894, 2016.

Yin, X.M., Dai, T., Xin, J.Y., Gong, D.Y., Yang, J., Teruyuki, N., Shi, G.Y.:

1082   Estimation of aerosol properties over the Chinese desert region with MODIS

1083   AOD assimilation in a global model, Adv. Clim. Change Res., 7, 90–98, 2016.

1084   Zhang, J., Reid, J. S., Westphal, D., Baker, N., and Hyer, E.: A System for

1085   Operational Aerosol Optical Depth Data Assimilation over Global Oceans, J.

1086   Geophys. Res., 113, D10208, doi:10.1029/2007JD009065, 2008.

1087   Zhang, Q., Streets, D. G., Carmichael, G. R., He, K. B., Huo, H., Kannari, A.,

1088   Klimont, Z., Park, I. S., Reddy, S., Fu, J. S., Chen, D., Duan, L., Lei, Y., Wang,

1089   L. T., and Yao, Z. L.: Asian emissions in 2006 for the NASA INTEX-B mission,

1090   Atmos. Chem. Phys., 9, 5131-5153, doi:10.5194/acp-9-5131-2009, 2009.

1091   Zhang, L., Liu, L. C., Zhao, Y. H., Gong, S. L., Zhang, X. Y., Henze, D. K., Capps, S.

1092   L., Fu, T. M., Zhang, Q., and   Wang, Y. X.: Source attribution of particulate

1093   matter pollution over North China   with the   adjoint method, Environ.Res.Lett.,

1094   10, Artn 08401110.1088/1748-9326/10/8/084011, 2015.

1095   Zheng, B., Zhang, Q., Zhang, Y., He, K. B., Wang, K., Zheng, G.

1096   J., Duan, F. K., Ma, Y. L., and Kimoto, T.: Heterogeneous

1097   chemistry: a mechanism missing in current models to explain

1098   secondary inorganic aerosol formation during the January 2013 haze

1099   episode in North China, Atmos.Chem.Phys., 15, 2031-2049,

1100   10.5194/acp-15-2031-2015, 2015.

1101

1102

1147

1148 Figure 9. Time series of the hourly PM$_{2.5}$ obtained from observations (circle), analysis
1149 (blue line), control run (black line) and hourly output of 48-h forecast in three
1150 megacities: (a) Beijing; (c) Shanghai; and (e) Guangzhou in expJ and (b) Beijing; (d)
1151 Shanghai; and (f) Guangzhou in expC. See text in section 5.4.

1152

1153 Figure 10. Bias of surface PM$_{2.5}$ as a function of forecast range calculated against all
1154 the independent observations over the three sub-regions shown in figure 1: (a)
1155 Beijing–Tianjin–Hebei region; (c) Yangtze River delta; (e) Pearl River delta and
1156 RMSE over (b) Beijing–Tianjin–Hebei region; (d) Yangtze River delta; (f) Pearl
1157 River delta; (g) Normalized RMSE (assimilation divided by control) for expJ and (h)
1158 Normalized RMSE for expC. The 48-h forecasts were performed at each 0000 UTC
1159 from 6 to 16 October 2014 and the statistics were computed from 6 to 16 October.

1160

1161

1162

1163
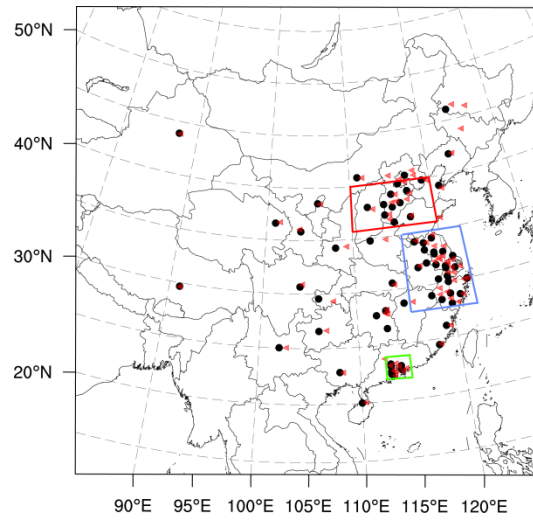
1164

Figure 1. Locations of 77 PM$_{2.5}$ assimilation observation stations (black dot) and the 77 independent observation stations (red triangle) in the model domain. The three colored boxes mark sub-regions with relatively dense coverage for the Beijing–Tianjin–Hebei region (JJJ, 12 assimilation stations and 12 independent stations, red box), the Yangtze River delta (YRD, 24 assimilation stations and 24 independent stations, blue box) and the Pearl River delta (PRD, 9 assimilation stations and 9 independent stations, green box).

1172

1173
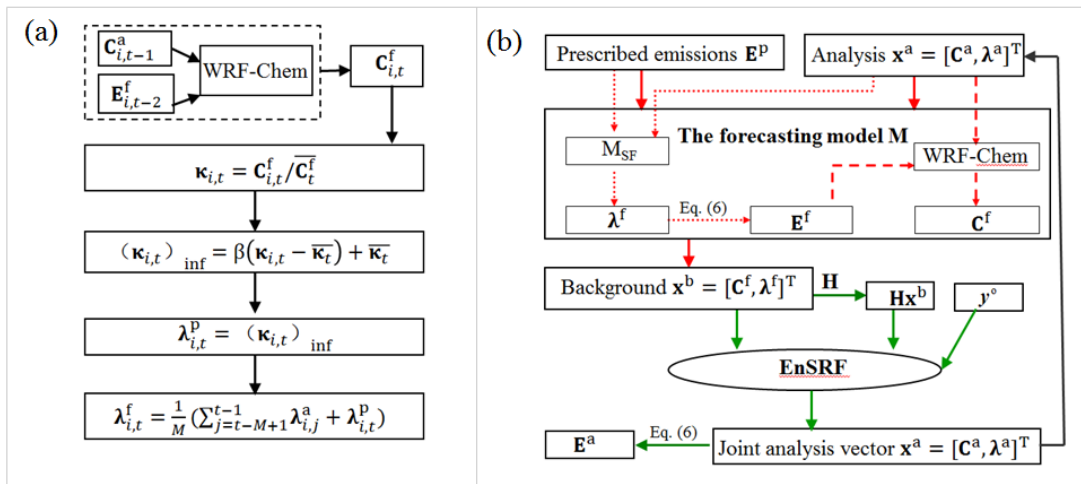
1174

1175 Figure 2. (a) Framework of $\mathbf{M}_{SF}$ and (b) flow chart of the data assimilation system
1176 that simultaneously optimizes the chemical initial conditions and emissions.

1177

1178

1179
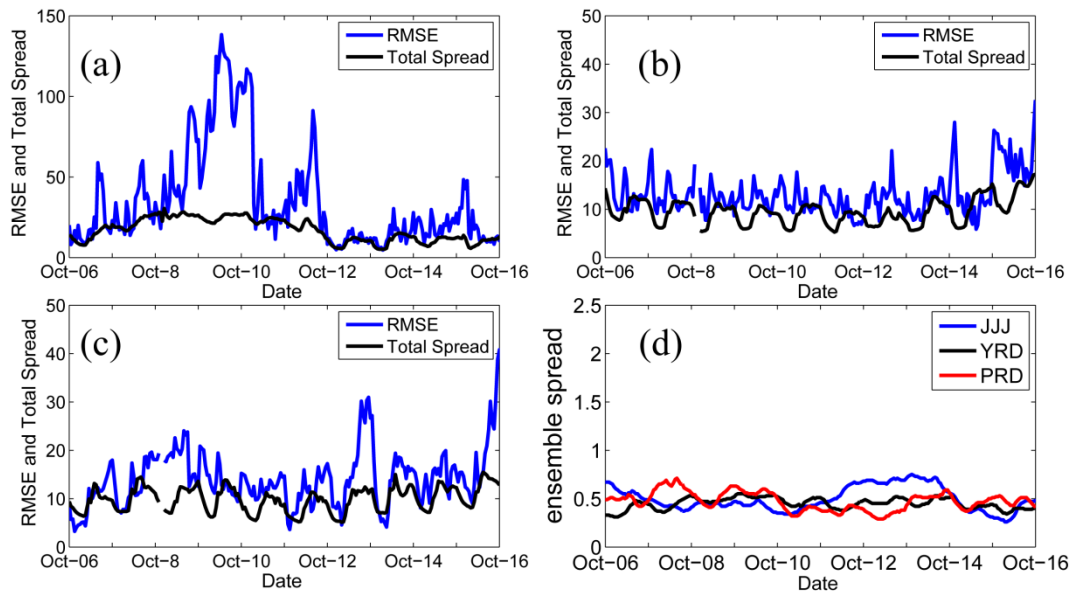
1180

1181   Figure 3. Time series of prior ensemble mean RMSE and total spread for PM$_{2.5}$

1182   concentrations aggregated over all observations over the three sub-regions: (a)

1183   Beijing–Tianjin–Hebei region; (b) Yangtze River delta; (c) Pearl River delta; and (d)

1184   time series of the area mean ensemble spread for $\lambda_{PM2.5}$ over the three sub-regions.

1185

1186

1187 Table 1. Comparison of the surface PM$_{2.5}$ mass concentrations from the control and
1188 assimilation experiments to observations over all analysis times from 6 to 16 October
1189 2014.

Region	Experiment	Mean observed value	Mean simulated value	BIAS	RMSE	CORR
Beijing–	Control		98.3	−18.0	81.6	0.790
Tianjin–	expJ	116.3	106.0	−10.3	66.9	0.827
Hebei	expC		104.1	-12.2	64.0	0.845
Yangtze	Control		64.4	15.9	30.6	0.593
River	expJ	48.5	46.9	-1.6	15.3	0.846
delta	expC		46.1	-2.4	17.3	0.803
Pearl	Control		82.4	20.6	31.8	0.624
River	expJ	61.8	66.5	4.7	16.1	0.800
delta	expC		64.1	-2.3	15.6	0.797

1190
1191
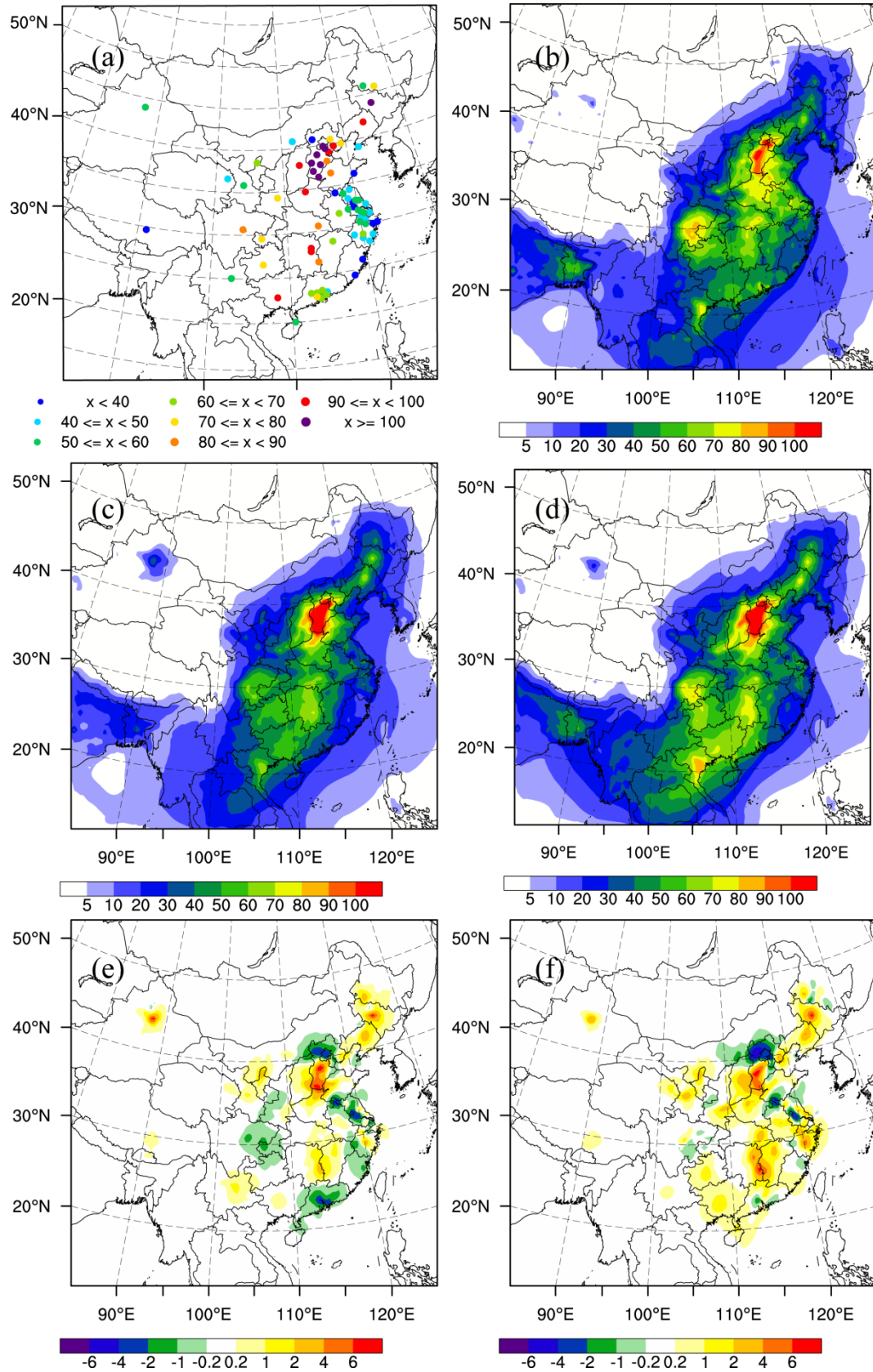
Figure 4. Spatial distribution of the PM$_{2.5}$ mass (μg m^{-3}) of the (a) observations; (b) simulation of the control run; (c) analysis of expJ; (d) analysis of expC; (e) increments of expJ; (f) increments of expC at the lowest model level averaged over all hours from

6 to 16 October 2014.

1197

1198

1199

Figure 5. Hourly area-averaged time series of emission scaling factors (black) extracted from the ensemble mean of the analyzed $\boldsymbol{\lambda}_{\mathrm{PM2.5}}^{\mathrm{a}}$ and the corresponding analyzed unspeciated primary PM$_{2.5}$ emissions $\mathbf{E}_{\mathrm{PM2.5}}^{\mathrm{a}}$ (blue) over the three sub-regions: (a) Beijing–Tianjin–Hebei region; (b) Yangtze River delta; and (c) Pearl River delta.
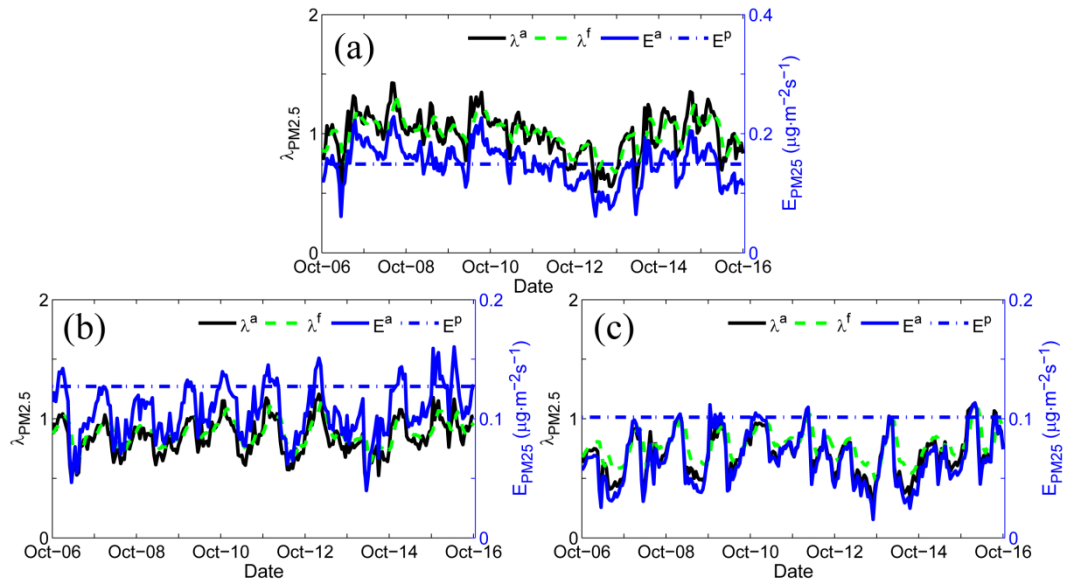
1200

1201

1202

1203

1204

1205

1206
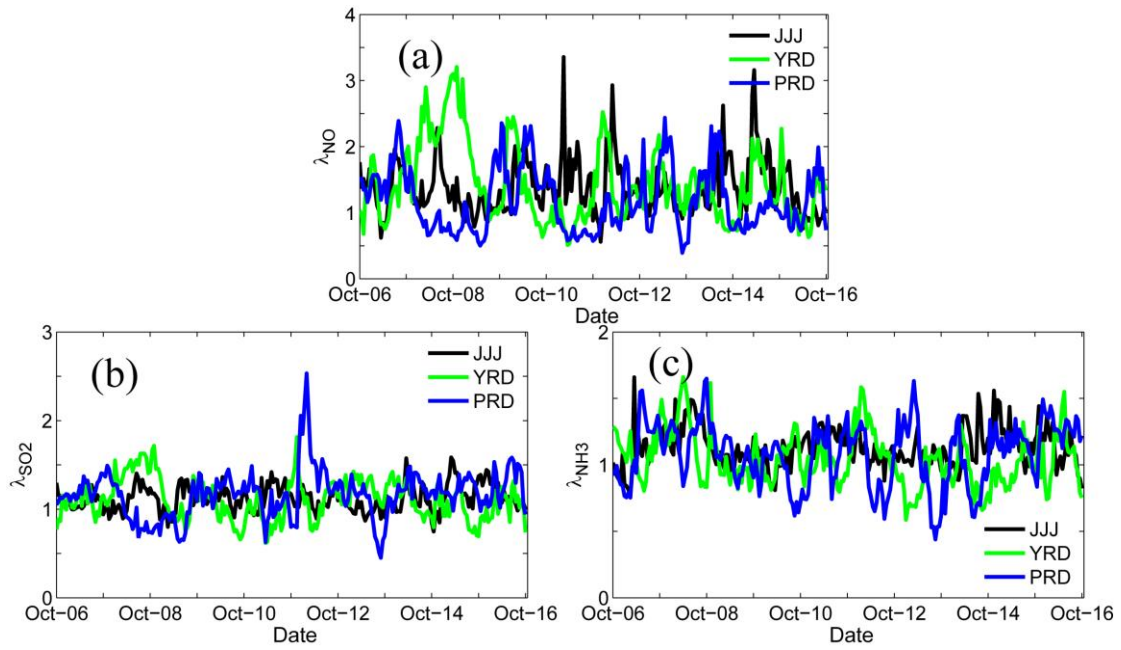
1207

1208   Figure 6. Hourly area-averaged time series of emission scaling factors extracted from

1209   the ensemble mean of the analyzed (a) λ_{NO}^{a}; (b) λ_{SO2}^{a}; (c) λ_{NH3}^{a} over the three

1210   sub-regions: Beijing–Tianjin–Hebei region (JJJ, black), Yangtze River delta (YRD,

1211   green), and Pearl River delta (PRD, blue).

1214
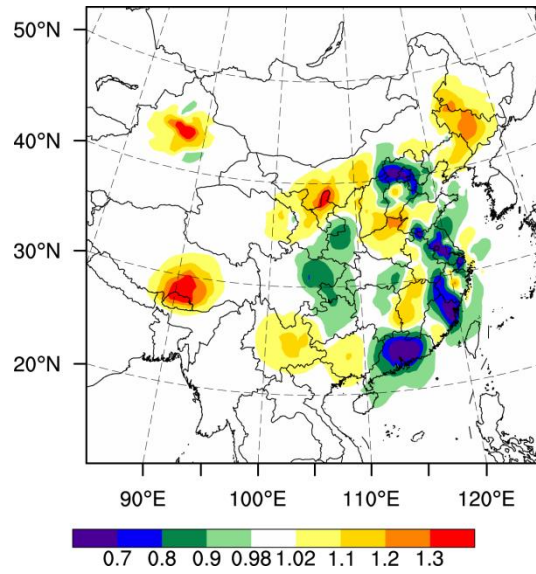
Figure 7. Spatial distribution of $\lambda_{PM2.5}$ at the lowest model level averaged over all hours from 6 to 16 October 2014.

1217
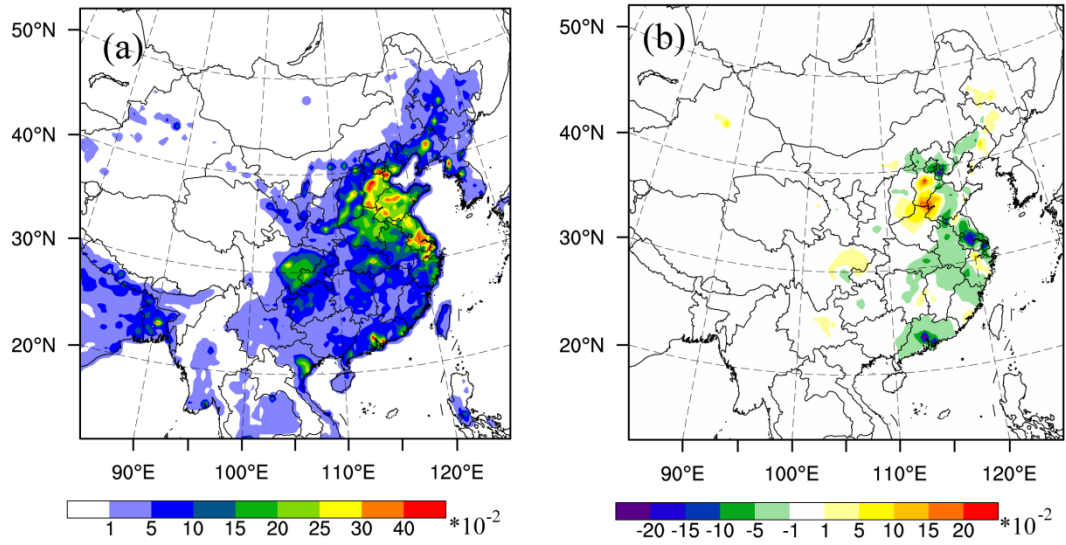
1218

1219   Figure 8. Spatial distribution of (a) the prior unspeciated primary sources of PM$_{2.5}$

1220   (μg m^{-2} s^{-1}) and (b) the time-averaged differences between the ensemble mean

1221 analysis and the prior values (μg ·m^{-2} s^{-1}) at the lowest model level averaged over all

1222   hours from 6 to 16 October 2014.
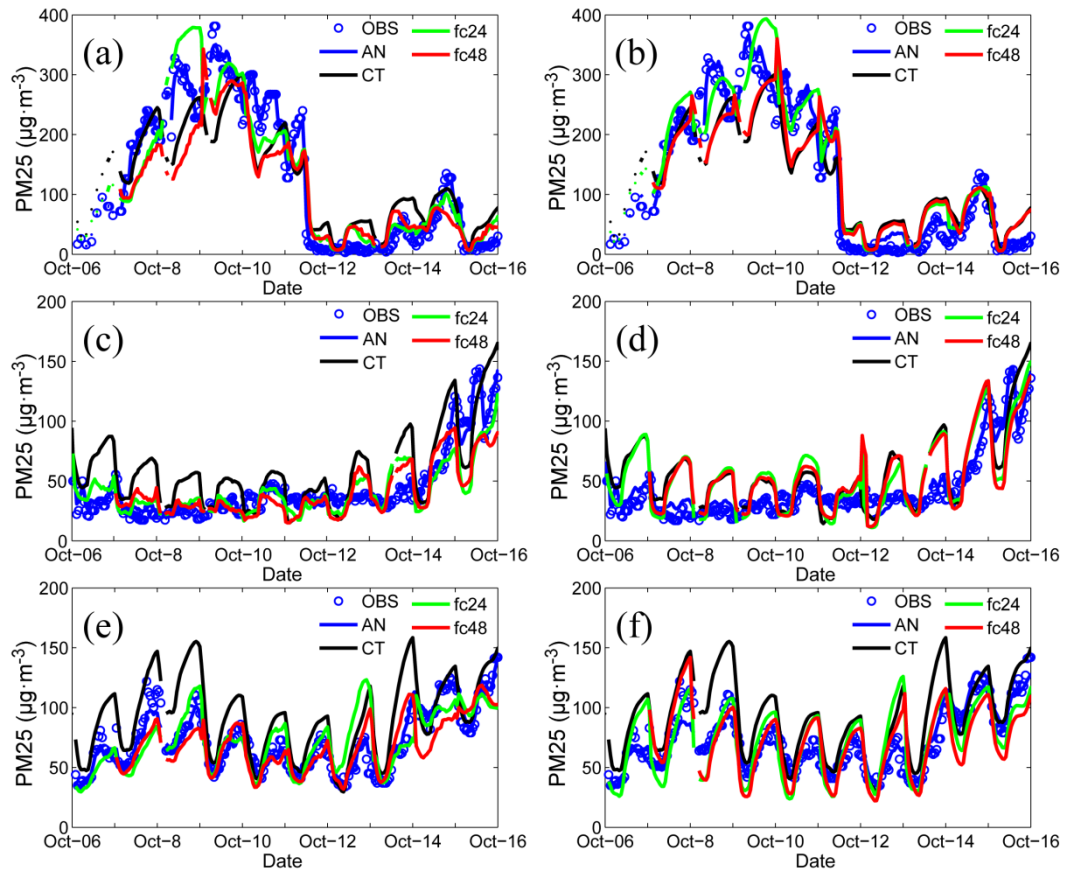
1223

1224 Figure 9. Time series of the hourly PM$_{2.5}$ obtained from observations (circle), analysis

1225   (blue line), control run (black line) and hourly output of 48-h forecast in three

1226 megacities: (a) Beijing; (c) Shanghai; and (e) Guangzhou in expJ and (b) Beijing; (d)

1227   Shanghai; and (f) Guangzhou in expC. See text in section 5.4.

1228

1229

1230

1231

1232   Figure 10. Bias of surface PM$_{2.5}$ as a function of forecast range calculated against all
1233   the independent observations over the three sub-regions shown in figure 1: (a)
1234   Beijing–Tianjin–Hebei region; (c) Yangtze River delta; (e) Pearl River delta and
1235   RMSE over (b) Beijing–Tianjin–Hebei region; (d) Yangtze River delta; (f) Pearl
1236   River delta; (g) Normalized RMSE (assimilation divided by control) for expJ and (h)
1237   Normalized RMSE for expC. The 48-h forecasts were performed at each 0000 UTC
1238   from 6 to 16 October 2014 and the statistics were computed from 6 to 16 October.

1239